

The Dynamical Simulation of the NCAR Community Climate Model Version 3 (CCM3)*

JAMES W. HURRELL, JAMES J. HACK, BYRON A. BOVILLE, DAVID L. WILLIAMSON, AND JEFFREY T. KIEHL

National Center for Atmospheric Research,⁺ Boulder, Colorado

(Manuscript received 12 May 1997, in final form 15 July 1997)

ABSTRACT

The dynamical simulation of the standard configuration of the latest version of the National Center for Atmospheric Research (NCAR) Community Climate Model (CCM3) is examined, including the seasonal variation of its mean state and its intraseasonal and interannual variability. A 15-yr integration in which the model is forced with observed monthly varying sea surface temperatures (SSTs) since 1979 is compared to coexisting observations. Results show that the most serious systematic errors in previous NCAR CCM versions have either been eliminated or substantially reduced.

At sea level, CCM3 reproduces the basic observed patterns of the pressure field very well. Simulated surface pressures are higher than observed over the subtropics, however, an error consistent with an easterly bias in the simulated trade winds and low-latitude surface wind stress. Amplitude errors and phase shifts of the subpolar low pressure centers over both hemispheres during winter produce the largest regional errors, which are on the order of 5 mb. In the upper troposphere, both the amplitude and location of the major circulation centers are very well captured by the model, in agreement with relatively small regional biases in the simulated winds. Errors in the zonal wind component at 200 mb are most notable between 40° and 50° lat of both hemispheres, where the modeled westerlies are stronger than observed especially over the Southern Hemisphere during winter. A ~50% reduction in the magnitude of the zonally averaged westerly bias in the equatorial upper troposphere that plagued previous CCM versions can be attributed to a significantly improved tropical hydrologic cycle and reduced Walker circulation.

Over middle latitudes, the CCM3 realistically depicts the main storm tracks, although the transient kinetic energy is generally underestimated, especially over the summer hemispheres. Over lower latitudes, the model simulates tropical intraseasonal oscillations with marked seasonality in their occurrence. Typical periodicities, however, are near 20–30 days, which are shorter than observed, and the simulated amplitudes are weaker than in both observations and previous versions of the model. The simulated response to interannual variations in tropical SSTs is also realistic in CCM3. A simulated index of the Southern Oscillation agrees well with the observed, and the model captures the overall structure and magnitude of observed shifts in tropical and subtropical convergence zones and monthly rainfall anomalies associated with the tropical SST changes.

1. Introduction

The National Center for Atmospheric Research (NCAR) Community Climate Model (CCM), a three-dimensional global atmospheric general circulation model (AGCM), has been utilized by many university and NCAR scientists to study the earth's climate system. The latest version of the CCM (CCM3) was made available to the scientific community in May 1996. Moreover, CCM3 is a central component of version 1 of the NCAR Climate System Model (CSM1), which is also available

for community use and includes component models for the ocean and sea ice as well (Boville and Gent 1998). The purpose of this paper is to document the climatological behavior of the standard configuration of CCM3, including the seasonal variation of its mean state and its intraseasonal and interannual variability. Results from an integration performed with the observed monthly varying mean sea surface temperatures (SSTs) since 1979 are compared to contemporaneous observations. The emphasis is on the dynamical representation of CCM3. Kiehl et al. (1998a) provide a detailed description of the model's radiative budget, Hack et al. (1998) describe its hydrologic cycle and thermodynamic structure, and Briegleb (1998) examines the polar climate of the model.

The outline of the paper is as follows. A brief description of CCM3 is presented in the next section, and the validation datasets are discussed in section 3. Comparisons to observations are made in section 4, including overviews of the general features of the simulated pressure, wind, and precipitation fields. A summary of the

* An electronic supplement to this article may be found on the CD-ROM accompanying this issue or at <http://www.ametsoc.org/AMS>.

⁺ The National Center for Atmospheric Research is sponsored by the National Science Foundation.

Corresponding author address: Dr. James W. Hurrell, NCAR/CGD, P.O. Box 3000, Boulder, CO 80307-3000.
E-mail: jhurrell@ncar.ucar.edu

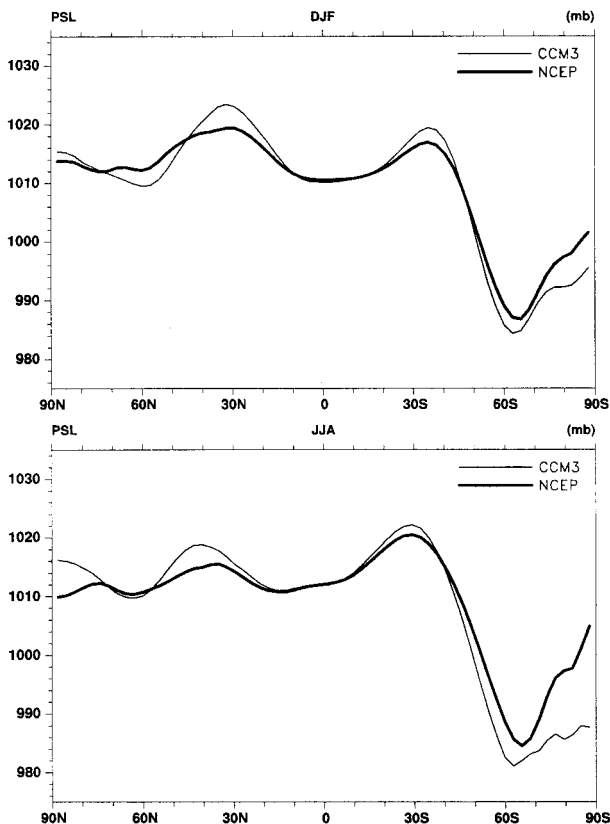


FIG. 1. Zonally averaged mean sea level pressure (mb) for DJF (top) and JJA (bottom) from CCM3 (thin solid) and NCEP (heavy solid).

primary simulation strengths and deficiencies of CCM3 is given in section 5.

2. Overview of CCM3

The NCAR CCM3 is a global spectral climate model. Its standard configuration includes a T42 horizontal spectral resolution (approximately a $2.8^\circ \times 2.8^\circ$ transform grid), 18 vertical levels, a top at 2.917 mb, and a time step of 20 min. A complete description of the physical and numerical methods used in CCM3 is provided by Kiehl et al. (1996).

The development of the CCM3 was motivated by the need to address the more serious systematic errors apparent in CCM2 simulations, as well as to make the model more suitable for coupling in the CSM. The major deficiencies in CCM2 simulations include a large warm and moist bias over the Northern Hemisphere (NH) middle and high latitudes during summer, sizeable amplitude errors and phase shifts in stationary wave patterns, a systematic overprediction of precipitation maxima especially over warm land, and cold polar tropopause temperatures (e.g., Hurrell et al. 1993; Hack et al. 1994). Kiehl et al. (1998b) summarize key differences between CCM3 and CCM2 simulations.

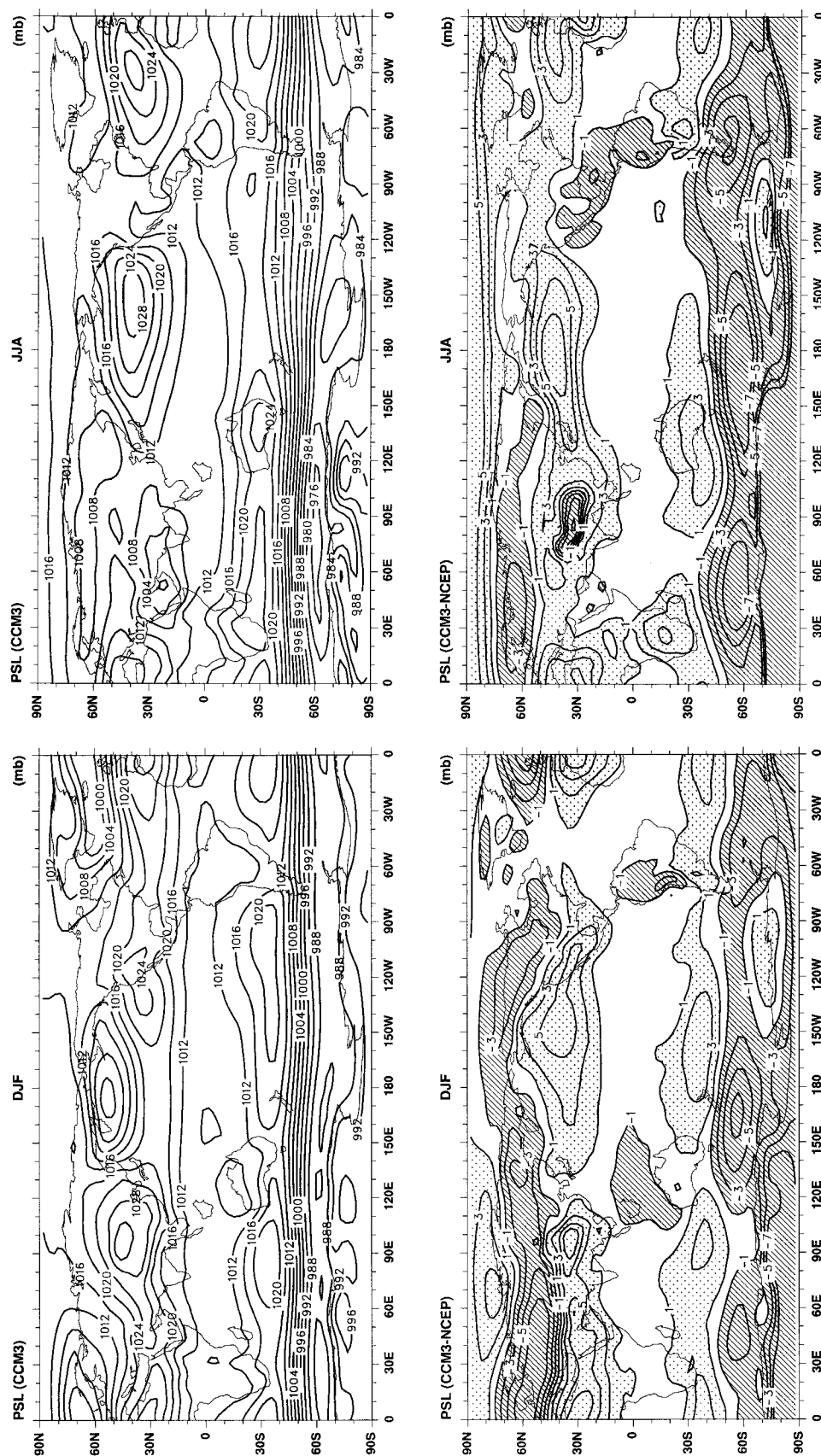
Modifications to the physical representation of specific climate processes in the CCM3 fall into five major categories: changes to the representation of radiative transfer through both clear and cloudy atmospheric columns, changes to the atmospheric boundary layer, moist convection and surface energy exchange, the incorporation of a sophisticated land surface model, the incorporation of an optional slab mixed layer ocean–thermodynamic sea–ice component, and a collection of other changes to the model formalism, which do not introduce significant changes to the model climate (Kiehl et al. 1996).

Changes to the clear-sky radiation formalism include the incorporation of trace gases (CH_4 , N_2O , CFC11, CFC12) in the longwave parameterization and the incorporation of a background aerosol (0.14 optical depth) in the shortwave parameterization. All-sky changes include improvements to the way in which cloud optical properties (effective radius and liquid water path) are diagnosed, incorporation of the radiative properties of ice clouds, and several other more minor modifications to the parameterization of convective and layered cloud amount. Systematic biases in the global annually averaged clear-sky and all-sky outgoing longwave radiation and absorbed solar radiation are substantially reduced to well within observational uncertainty, while maintaining very good agreement with global observational estimates of cloud forcing as a result of these changes (Kiehl et al. 1998a). Additionally, the large warm bias in simulated NH summer land temperature, the overprediction of precipitation over warm land, and a component of the stationary wave error in CCM2 are reduced as a result of the cloud-radiation improvements (Kiehl et al. 1998b).

Modifications to the atmospheric boundary layer formulation in CCM3 result in improved estimates of the boundary layer height. Parameterized convection has also been modified and is now represented using the deep moist convection formalism of Zhang and McFarlane (1995) in conjunction with the scheme developed by Hack (1994) for CCM2. The combination of the boundary layer and convection changes, the incorporation of a Sundqvist (1988) style evaporation of stratiform precipitation, and the incorporation of a new Land Surface Model (LSM) result in a 14% reduction in the global latent heat flux and associated global precipitation rate, a smoother distribution of tropical precipitation, and a further improvement in the stationary wave pattern relative to CCM2 (section 4; see also Hack et al. 1998; Kiehl et al. 1998b). The LSM, which replaces the prescribed surface wetness, snow cover, and soil wetness in CCM2, is a one-dimensional model of energy, momentum, water, and CO_2 exchange between the atmosphere and land (Bonan 1996).

3. Validation data

Many different fields are examined in an attempt to gain a fairly complete view of the dynamical simulation.



The primary source of validation data is the National Centers for Environmental Prediction (NCEP) global reanalyses (Kalnay et al. 1996). The archive used here consists of twice-daily analyses at 17 pressure levels in the vertical. Fifteen-year (1979–93) December–February (DJF) and June–August (JJA) climatologies were constructed from this archive, and the results were truncated from T63 to T42 resolution for comparison to the pressure-interpolated fields from CCM3.

Estimates of seasonal-mean precipitation rates were taken from the data of Xie and Arkin (1996). The global gridded fields of monthly precipitation since 1979 were constructed by combining estimates from gauge observations, three types of satellite estimates, and predictions from the European Centre for Medium-Range Weather Forecasts (ECMWF) operational forecast model. The result is a product that well represents with reasonable amplitude the large-scale spatial patterns, both over the Tropics and the extratropics. However, as Xie and Arkin (1996) caution, the actual quality of the merged product depends highly on the uncertain error structures of the individual data sources, so comparisons to CCM3 should be viewed as qualitative, not quantitative.

Finally, a surface field important for coupling is the surface momentum flux, or wind stress, by which the atmospheric winds drive the surface ocean currents. The observed climatological data used here are from Trenberth et al. (1990). They computed 7 yr (1980–86) of monthly mean wind stresses from twice-daily globally analyzed 1000-mb wind fields from ECMWF, which provided much better coverage and temporal sampling over much of the world's oceans than conventional ship data alone. Consequently, the wind stress statistics over the southern oceans are believed to be the most reliable, and the stresses are much larger than those documented in earlier climatologies. The main problems appear in the Tropics where the divergent component of the wind assumes a more important role. In these regions, uncertainties arise because of operational changes in the analysis–forecast system over time (see Trenberth 1992).

4. Results

Most results are presented in two-panel figures for both mean DJF and JJA 15-yr (1979–93) simulated climates. The format is to present the data from CCM3 in the top panel and either observations or differences from observations (e.g., CCM3 minus NCEP) in the lower panel. Zonal averages of single-level fields are presented as line plots with DJF in the top panel and JJA in the lower panel. For surface wind stress, CCM3 results were averaged over the period 1980–86 for compatibility with the climatology of Trenberth et al. (1990).

a. Sea level pressure

The mean sea level pressure (SLP) pattern is a useful indication of an AGCM's ability to simulate the atmospheric circulation near the surface, and it represents an integrated measure of a model's thermodynamic and dynamic representations. The zonally averaged SLP fields are shown in Fig. 1, and the spatial distribution of seasonal means and differences from the NCEP reanalyses are presented in Figs. 2 and 3. Because of the sea level reduction problem, the magnitude of differences over regions of high topography (e.g., the Himalayas, Greenland, the Andes, and Antarctica) are not meaningful.

The model reproduces the basic observed patterns quite well. Interseasonal differences are most striking in the NH where the subtropical high pressure centers are especially well developed during northern summer and the high-latitude Aleutian and Icelandic low pressure systems intensify during winter in the CCM3, as observed. The model also captures the largest seasonal pressure variations in the NH, which are found over the Asian continent and are related to the development of the Siberian anticyclone during winter and the monsoon low over Southeast Asia during summer (Figs. 2 and 3). Over the Southern Hemisphere (SH), the SLP from CCM3 rises from a nearly continuous low pressure zone near the equator (the intertropical convergence zone, ITCZ) to a circumpolar peak in the subtropics where there is an anticyclone center in each ocean, in good agreement with observations. The subtropical belt of high pressure also lies a few degrees latitude farther poleward and is weaker during southern summer than winter in both the CCM3 and NCEP data (Fig. 1), so that the oceanic subtropical highs over both hemispheres reach their peaks during JJA (Fig. 3). Farther poleward, the mean SLP rapidly drops to its lowest values in the circumpolar trough between 60°S and 70°S. The zonally averaged pressure in the circumpolar trough is about 4 mb higher in southern summer than winter (Fig. 1) in the CCM3, again in good agreement with the observations.

Significant regional biases, however, are noticeable in the difference plots, although generally much smaller in magnitude than in earlier versions of the CCM (Hurrell et al. 1993). During northern winter, SLPs throughout the subtropics of both hemispheres are higher than observed, whereas pressures in subpolar latitudes are too low (Fig. 1). The Aleutian low does not extend as far east and south as observed, which contributes to a positive difference of more than 5 mb over the eastern Pacific (Fig. 2). The SLP distribution over the northern Atlantic Ocean is well simulated by CCM3, although the high pressure ridge becomes too strong over northern Africa and differences of similar magnitude extend across the Middle East into Asia. The central pressure of the Icelandic low during DJF is in good agreement with the NCEP data, but the center of the low is not

closed off and erroneously low pressures extend across northern Europe well into Eurasia. Over the SH, the positions of the summertime subtropical ridges to the west of the continents are well represented although shifted slightly poleward. The model does not capture the observed asymmetries in the SH subtropical highs in which the pressure centers are shifted eastward toward the continents. The circumpolar Antarctic trough is well positioned (Fig. 1), yet the central pressures are generally deeper than observed, resulting in a modestly stronger meridional gradient on the equatorward side of the trough (Fig. 2). The largest differences at these latitudes are more than -7 mb south of New Zealand and are associated with the model's inadequate weakening and poleward shift of the maximum meridional pressure gradient over the Pacific. This notable feature of the SH climate (e.g., van Loon 1972; Hurrell et al. 1998) gives rise to the dominance of wavenumber 1 at middle and high latitudes (see also Fig. 7; Raphael 1998).

During southern winter (Fig. 3), the CCM3 SLP errors in high SH latitudes are larger than during summer and result from the circumpolar trough being too deep and too far equatorward (Fig. 1), typical of earlier versions of the CCM as well (Hurrell et al. 1993). Although the model simulates a weakened meridional pressure gradient over the eastern Pacific, the observed changes are closer to the date line so again large differences from the NCEP reanalyses are found south of New Zealand. Over the NH, the summer subtropical ridges over the Pacific and Atlantic in CCM3 are too strong and are shifted slightly poleward relative to observations. In particular, the central pressure of the Azores high during JJA is near 1028 mb in CCM3, compared to ~ 1024 mb in the NCEP data, and it is located nearly 5° lat too far to the north. Similar errors in the central pressure and location are notable with the Pacific high, which also erroneously extends too far to the west resulting in differences from NCEP data of more than 7 mb over the central Pacific (Fig. 3).

b. Geopotential height

A representative climate parameter of the midtropospheric flow is the 500-mb geopotential height field (Figs. 4, 5, and 6). Many of the same characteristics seen in the SLP plots are evident at 500 mb as well. The model captures the interseasonal shifts in the mean positions of the tropical ridges (Fig. 4), which during DJF are about 10° lat south of their positions during JJA, and during both seasons they are equatorward of their positions at sea level (Fig. 1). Both the simulated and observed 500-mb height profiles (Fig. 4) have a larger latitudinal gradient in the SH than in the NH during the summer seasons. The zonal means of the hemispheres differ less during the two winter seasons in CCM3, as in observations.

Locally, the model captures the major troughs off the east coasts of Asia and North America during northern

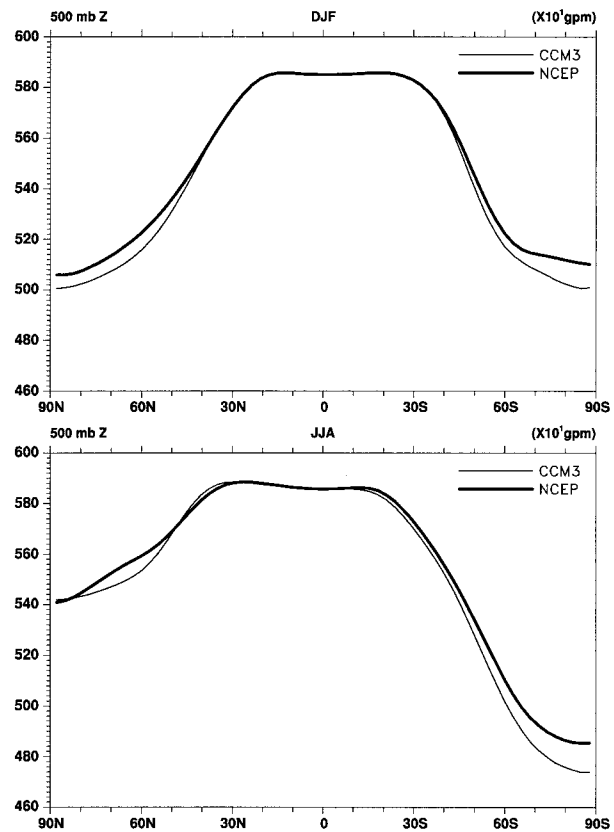


FIG. 4. Zonally averaged mean 500-mb geopotential height (10^1 gpm) for DJF (top) and JJA (bottom) from CCM3 (thin solid) and NCEP (heavy solid).

winter, in addition to the trough over eastern Europe (Fig. 5). The ridges over Russia, the west coast of North America, and the eastern Atlantic are also well simulated. Over the SH, as observed, the 500-mb height gradient is weaker in the middle latitudes of the Pacific Ocean than in the same latitudes elsewhere during both seasons (Figs. 5 and 6), which gives rise to a pattern of zonally asymmetric heights dominated by wavenumber 1 (e.g., van Loon 1972). In the CCM3, as in the NCEP data, the locations of the zonal asymmetries at middle and high SH latitudes are the same in both seasons, but the amplitudes of the anomalies are larger during southern winter (see also Raphael 1998).

Consistent with a slight cold bias at extratropical latitudes in CCM3 (Hack et al. 1998), simulated middle tropospheric heights are lower than observed at high latitudes of both hemispheres during DJF, and are lower throughout most of the SH during JJA (Fig. 4). Part of this bias at high latitudes of the SH is caused by an overspecification of sea ice in the CCM3 boundary conditions for this simulation. In CSM1, for example, the predicted fractional ice coverage and ice thickness are much closer to observed values, and the CSM atmosphere warms relative to CCM3 by up to 7°C in the

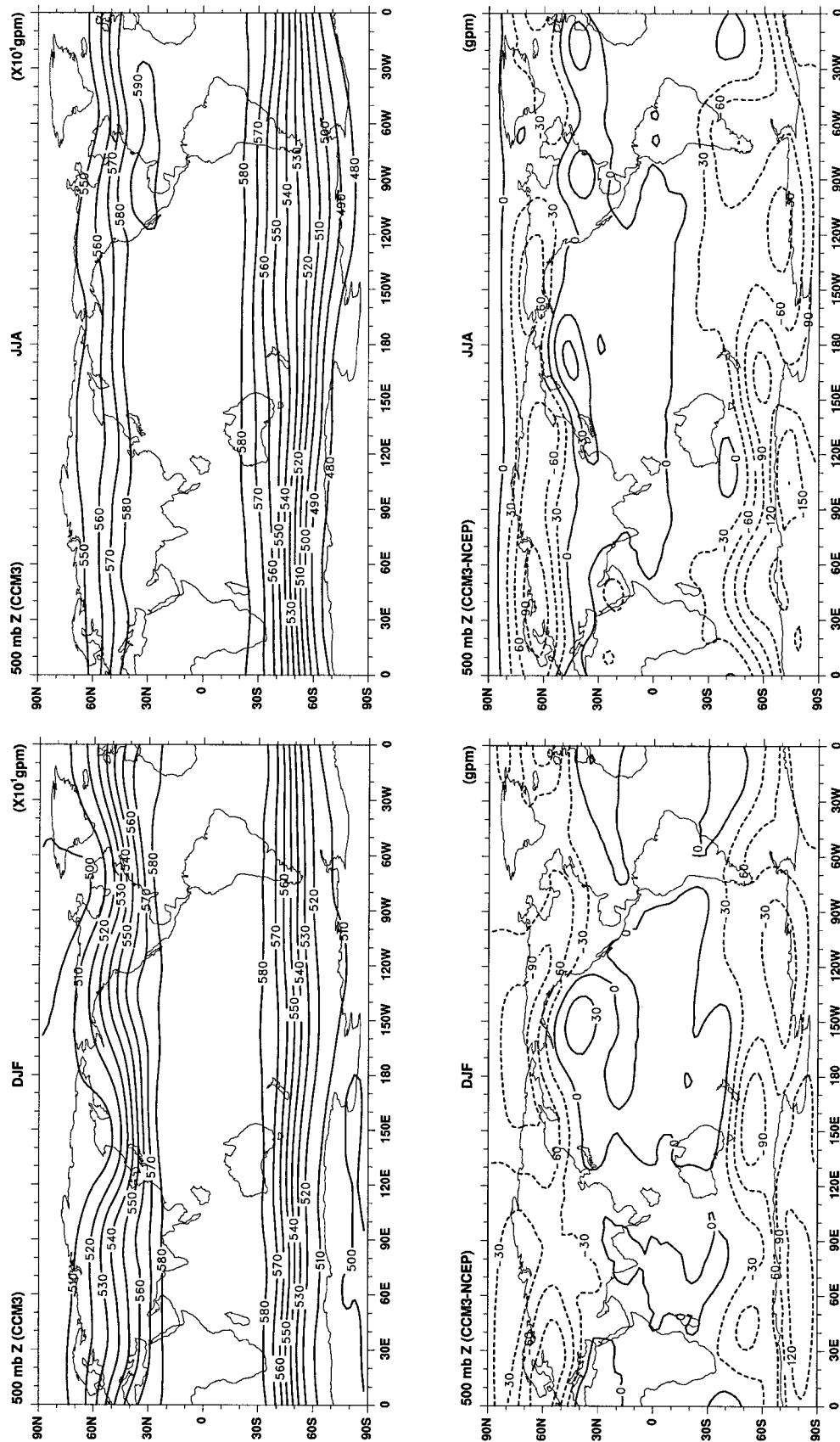


FIG. 6. As in Fig. 5 but for JJA.

FIG. 5. Mean DJF 500-mb geopotential height from CCM3 (top) and differences from the NCEP climatology (bottom). The contour increment in the top panel is 100 gpm. Differences are contoured every 30 gpm and negative values are dashed.

lower troposphere around Antarctica (Boville and Hurrell 1998).

Regional differences from the NCEP reanalyses (Figs. 5 and 6) are largely consistent with the SLP errors discussed earlier, and again are considerably smaller than in earlier CCM versions (Hurrell et al. 1993). The ridge over the west coast of North America during DJF is shifted just to the west of the observed location at 500 mb, resulting in an error of ~ 30 gpm over the Pacific with negative height differences over western Canada. Over Europe, differences of -90 gpm reflect a simulated Atlantic ridge that does not extend as far east as observed and is too weak. The 500-mb height biases over the SH are consistent with biases in the simulation of the circumpolar trough noted in Figs. 2 and 3.

Large-scale deviations from zonal means are described well by a Fourier decomposition of the geopotential heights along latitude circles. Raphael (1998) provides a detailed analysis of the SH quasi-stationary waves in CCM3 during DJF and JJA. The annual cycles of the amplitudes of waves 1–3 at 300 mb are presented in Figs. 7–9 for both the CCM3 and the NCEP reanalyses.

Over the SH, the amplitude of wave 1 reaches its peak between late winter and early spring in both the model and observations, although the simulated amplitudes are too large (Fig. 7). The model also simulates the observed slight poleward movement of maximum amplitudes from southern summer into winter. The phase of wave 1 over the subantarctic remains the same through the year in both the CCM3 and NCEP data (not shown), although it is shifted eastward in the model by about 25° long. More than 80% of the mean spatial variance is explained by wave 1 in DJF and JJA in CCM3, as in observations (see Raphael 1998). Note also that the CCM3 captures the observed second peak in the amplitude of wave 1 between 30°S and 40°S , which is largest in winter. Wave 2 over the SH is comparatively small in both CCM3 and observations (Fig. 8), reaching its maximum of more than 40 gpm over the antarctic during the colder part of the year. Wave 3 over the SH is also small in comparison with wave 1. The observed amplitude of wave 3 between 50°S and 60°S is more than 40 gpm during southern summer and is only slightly less in winter, features not well simulated by CCM3 (Fig. 9). However, it is important to note that the amplitude of wave 3 at high SH latitudes varies considerably from one year to another (e.g., van Loon et al. 1993), so the results could be sensitive to sampling of natural internal atmospheric variability.

The interseasonal changes in the quasi-stationary waves are larger over the NH in both CCM3 and observations. Wave 1 has a maximum amplitude of more than 160 gpm near 45°N during northern winter in the NCEP reanalyses (Fig. 7 bottom). The maximum amplitude in CCM3 is smaller, especially in early winter, but is also located near 45°N . The amplitude of wave 1 weakens from winter to summer to a maximum of

about 60 gpm near 70°N in both CCM3 and observations, although the simulated amplitude is too weak in northern spring. In contrast to the SH, wave 1 during winter over the NH is baroclinic leaning westward with height in both the model and observations (not shown), a feature evident in the higher zonal harmonic waves as well. Another well-simulated feature not evident in Fig. 7 is that near 30°N wave 1 has peaks in the upper (near 150 mb) and lower troposphere with a minimum near 500 mb (not shown). Both the simulated and observed phases reverse between the two peaks, reflecting the change in the monsoon over Asia from a low pressure center at sea level (Fig. 3) to a high pressure center in the upper troposphere. The monsoonal phase reversal with height is seen in waves 2 and 3 as well (not shown). Wave 2 at higher latitudes is much more pronounced over the NH than over the SH, and during northern winter its amplitude equals or exceeds wave 1. These aspects are well captured by CCM3 (Fig. 8). Wave 3 is also large over the NH during winter, but is too strong in CCM3 (Fig. 9). Both the simulated and observed amplitudes of waves 2 and 3 dwindle to near 20 gpm in summer.

Plots of the interannual variability of the winter and summer 500-mb heights (Figs. 10 and 11) show that the NH has a strong seasonal cycle with maximum variability during winter in the vicinities of the Aleutian and Icelandic lows. In both seasons the observed variability is zonally asymmetric over the SH and is largest in the Pacific, where the influence of the Southern Oscillation is strongest (e.g., van Loon 1984), with a secondary maximum over the Indian Ocean. Also, the interannual variability of the summertime flow is larger in the SH than in the NH. Overall the model captures these aspects quite well. Regional differences are, however, evident. Over the NH during DJF, the interannual variability is too large in CCM3 over much of the North Pacific and, unlike the observations, maximum values extend into western North America. Over the SH, interannual variations in 500-mb heights are generally underestimated during both seasons.

c. Wind

The horizontal wind distribution is closely linked geostrophically to the temperature and pressure distributions. The zonal wind, in particular, has traditionally been one of the fundamental climate simulation verification parameters. Overall, the zonal wind structure is well simulated (Figs. 12 and 13), preserving a strength of CCM2 not as evident in earlier versions of the NCAR CCM (e.g., Hurrell et al. 1993). The simulated mean zonal flow in the NH during winter is very similar to the NCEP winds equatorward of 40°N with the strongest westerlies near 40 m s^{-1} at the 200-mb level (Fig. 12). Between 40°N and 50°N , however, the zonally averaged westerlies in CCM3 are stronger than observed by a few meters per second, with a larger westerly bias evident

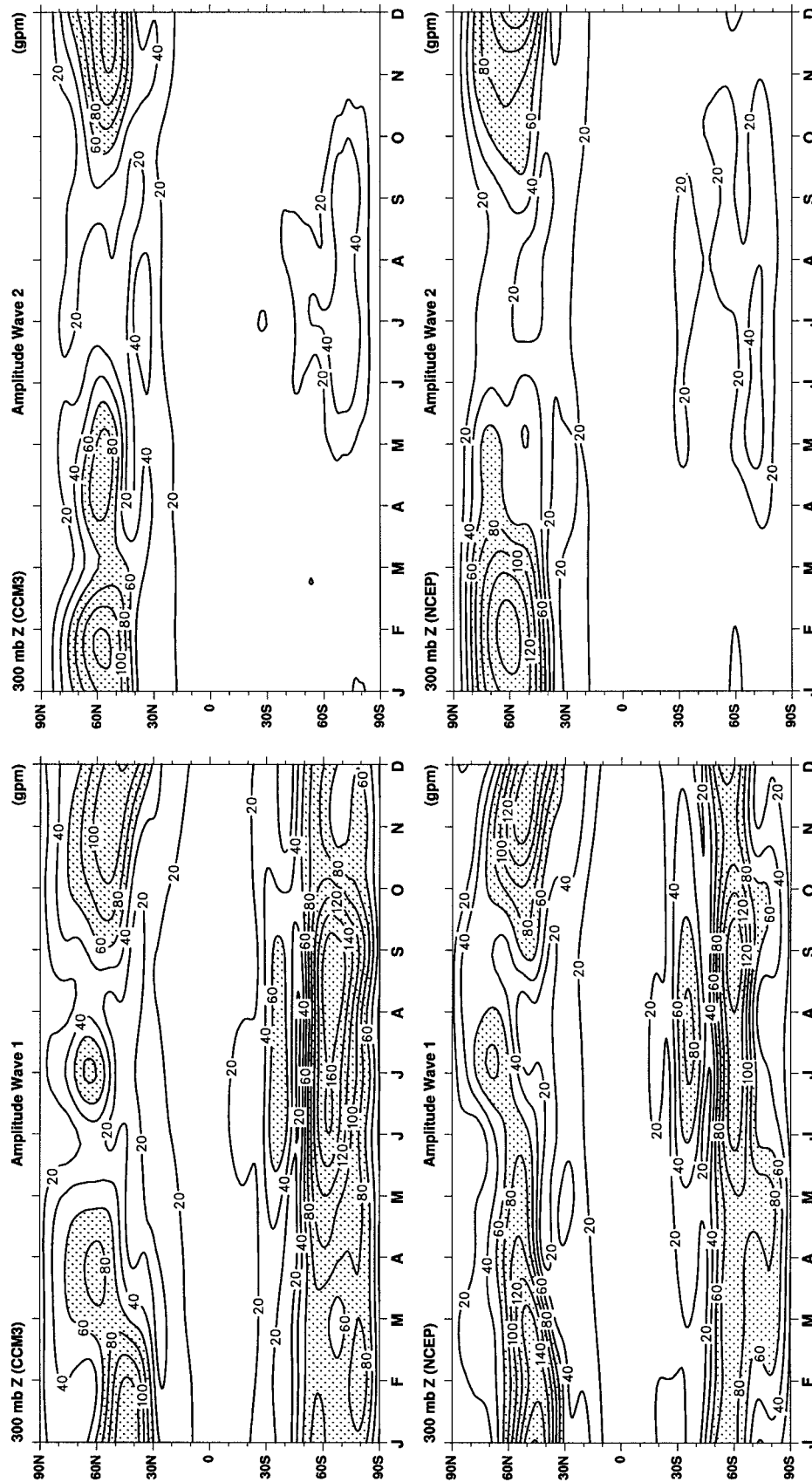


FIG. 7. The annual march of the amplitude of wavenumber 1 in 300-mb geopotential heights from CCM3 (top) and NCEP (bottom). The contour increment is 20 gpm and values greater than 60 gpm are stippled.

FIG. 8. As in Fig. 7 but for wavenumber 2.

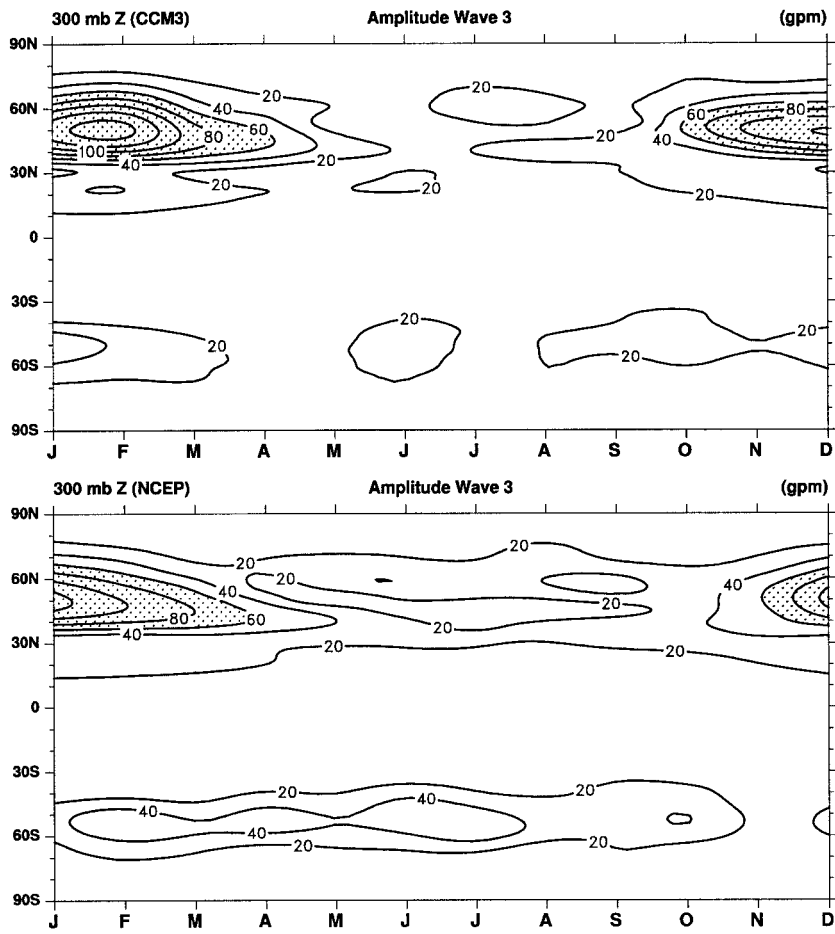


FIG. 9. As in Fig. 7 but for wavenumber 3.

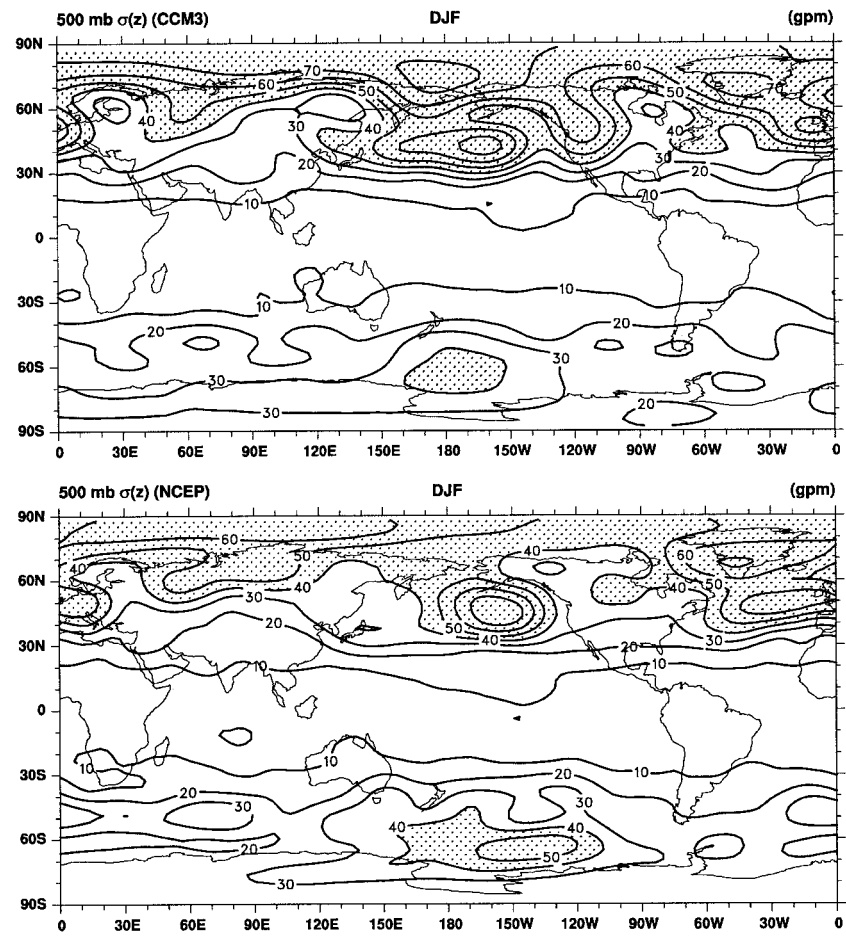


FIG. 10. The standard deviation of the 15 mean DJF 500-mb geopotential height fields from CCM3 (top) and NCEP (bottom). The contour increment is 10 gpm and values greater than 40 gpm are stippled.

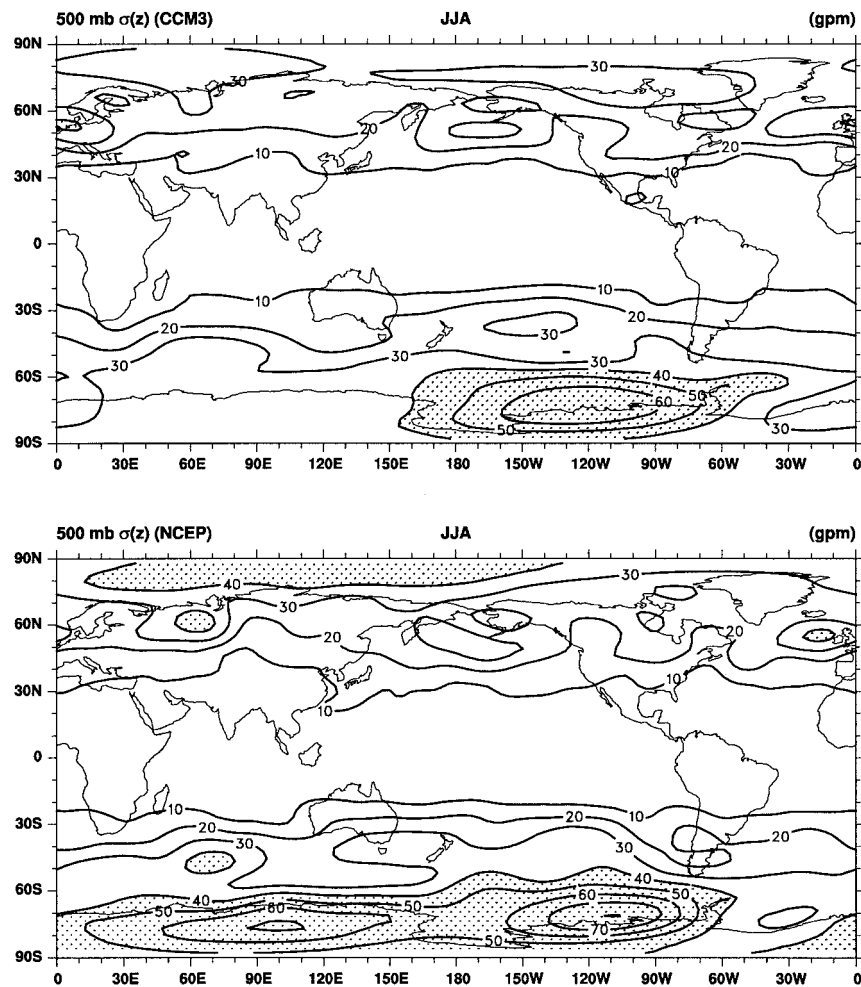


FIG. 11. As in Fig. 10 but for JJA.

during JJA (Fig. 13). Over the SH, as observed, the simulated upper-tropospheric middle-latitude maximum during winter is about 2° – 3° lat nearer the equator than its NH winter counterpart. But in contrast to observations, it is stronger than the NH winter maximum by about 5 m s^{-1} , contributing to large westerly bias. This bias also reflects another shortcoming of the SH winter simulation: the observed maximum near 30°S is clearly separated from a second westerly maximum in the upper troposphere that continues into the stratosphere, a feature not well captured by CCM3. A westerly bias is also evident at these latitudes and heights during southern summer.

In good agreement with observations, the simulated low-level easterlies are of nearly equal magnitude in each winter hemisphere and cover similar areas, and the upper-tropospheric tropical easterlies are much stronger in the NH than in the SH during summer. In earlier versions of the CCM, the summertime NH tropical easterlies were much too strong (by $\sim 8 \text{ m s}^{-1}$) and extended too far poleward (maximum easterly errors were between 20°N and 40°N), biases earlier identified by Boer

et al. (1991) as common to most AGCMs. The CCM3 simulation is much better in these respects (Fig. 13). Another persistent problem in earlier versions of the model was a westerly wind bias near the equator in the upper troposphere during both seasons. While this error remains, it has been reduced by nearly 50% in CCM3.

The regional distribution of the zonal wind at 850 mb (Figs. 14 and 15) illustrates that the major features of the zonal flow are well simulated by CCM3. During DJF, the model simulates westerly maxima off the east coasts of Asia and North America, although they are slightly stronger than observed (Fig. 14). This is especially true over the eastern Atlantic and across Europe, where the banded structure of zonal wind biases is consistent with the SLP errors noted earlier (see Fig. 2). The largest interseasonal changes over the NH reflect the interseasonal variations of the semipermanent surface pressure centers. The model captures the poleward shift (by $\sim 10^{\circ}$ lat) of the westerly maxima from winter to summer over the northern oceans; yet, the maxima are stronger than observed, and the simulated transition from westerlies to easterlies is located too far poleward

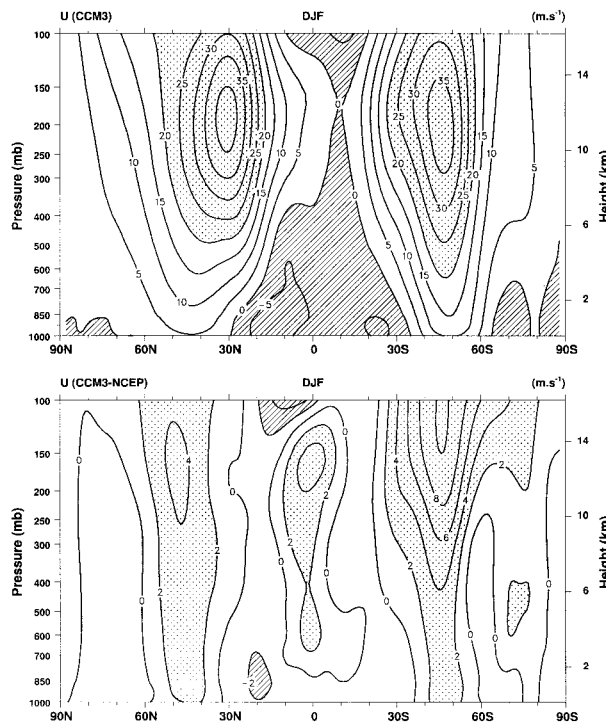


FIG. 12. Zonally averaged mean DJF zonal wind from CCM3 (top) and differences from the NCEP climatology (bottom). The contour increment in the top panel is 5 m s^{-1} , easterlies are hatched, and values greater than 20 m s^{-1} are stippled. Differences are contoured every 2 m s^{-1} , values less than -2 m s^{-1} are hatched, and differences greater than 2 m s^{-1} are stippled.

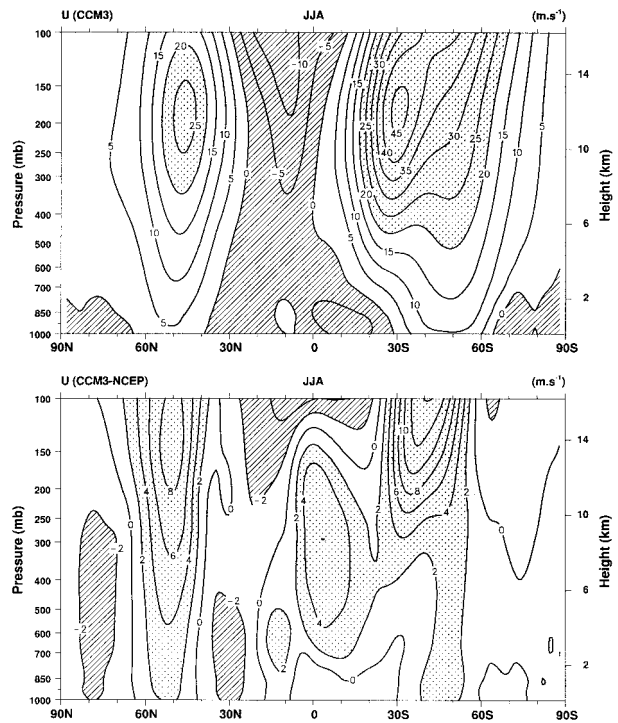


FIG. 13. As in Fig. 12 but for JJA.

over each ocean basin. The latter results in an easterly bias near 30°N in the zonal mean (Fig. 13) with a local maximum bias of -6 m s^{-1} over the subtropical western Pacific (Fig. 15). The large interseasonal changes associated with the summer and winter monsoons are generally well captured by CCM3, although the westerlies over the Bay of Bengal during JJA are not as strong as observed and the simulated easterlies to the south are too strong (Fig. 15). The simulated lower-tropospheric winds over the western tropical Pacific during northern winter have an easterly bias, although considerably improved over CCM2 (e.g., Hurrell et al. 1993). Over the SH, the strongest westerlies in the CCM3 are in the latitudes near 50°S in both summer and winter, in good agreement with the observations. Also as observed, they are weakest in the Pacific Ocean and reach a peak of more than 15 m s^{-1} in the Indian Ocean, reflecting the zonal asymmetry in pressure described earlier. The slight westerly bias at these latitudes is consistent with the SLP errors noted before, namely, the stronger-than-observed meridional pressure gradient on the equatorward side of the circumpolar trough, and the failure to simulate the observed zonal asymmetry in the pressure field south of New Zealand (Figs. 2 and 3).

In the upper troposphere the strongest westerlies occur over the NH during winter (Fig. 16) and reach more

than 60 m s^{-1} off the Asian coast and 40 m s^{-1} over the eastern United States and the western Atlantic. Westerlies extend across the equator over the Atlantic and central Pacific Oceans during northern winter, and over the SH the peak in the westerlies is reached between 40°S and 50°S with maxima over the Atlantic and Indian Oceans. All of these features are in very good agreement with the NCEP reanalyses, so that the differences in Fig. 16 are generally quite small and are a considerable improvement over earlier CCM versions (Hurrell et al. 1993; Kiehl et al. 1998b). The largest zonal wind errors during DJF are more than 10 m s^{-1} south of Australia extending east across New Zealand, although the model overestimates the strength of the SH westerlies throughout this latitude band.

During northern summer at 200-mb several notable features of the simulation are again in good agreement with the observations (Fig. 17). A closed circulation is evident over the southern part of Asia accompanied by a northward shift and substantial weakening of the higher-latitude westerly jet stream, although the simulated shift is too far poleward and the westerly maxima too strong. This results in a westerly error in the zonal average near 50°N (Fig. 13). Tropical easterlies nearly encircle the near-equatorial latitudes and are strongest over the Indian Ocean with peak values near -20 m s^{-1} (the tropical easterly jet), conforming to observations, but the simulated easterlies do not extend as far south as observed over the tropical Indian and western Pacific Oceans, contributing to a westerly bias of up to 10 m s^{-1} . Over the Atlantic off the coast of Africa, the

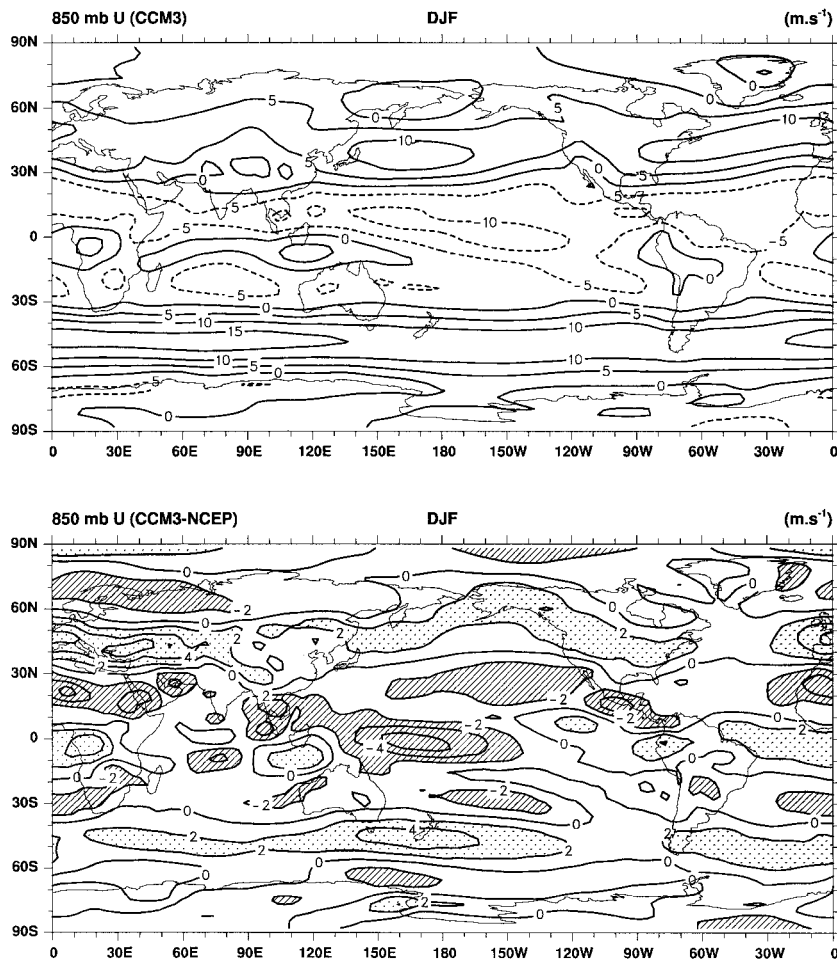


FIG. 14. Mean DJF 850-mb zonal wind from CCM3 (top) and differences from the NCEP climatology (bottom). The contour increment in the top panel is 5 m s^{-1} and easterlies are dashed. Differences are contoured every 2 m s^{-1} , values less than -2 m s^{-1} are hatched, and differences greater than 2 m s^{-1} are stippled.

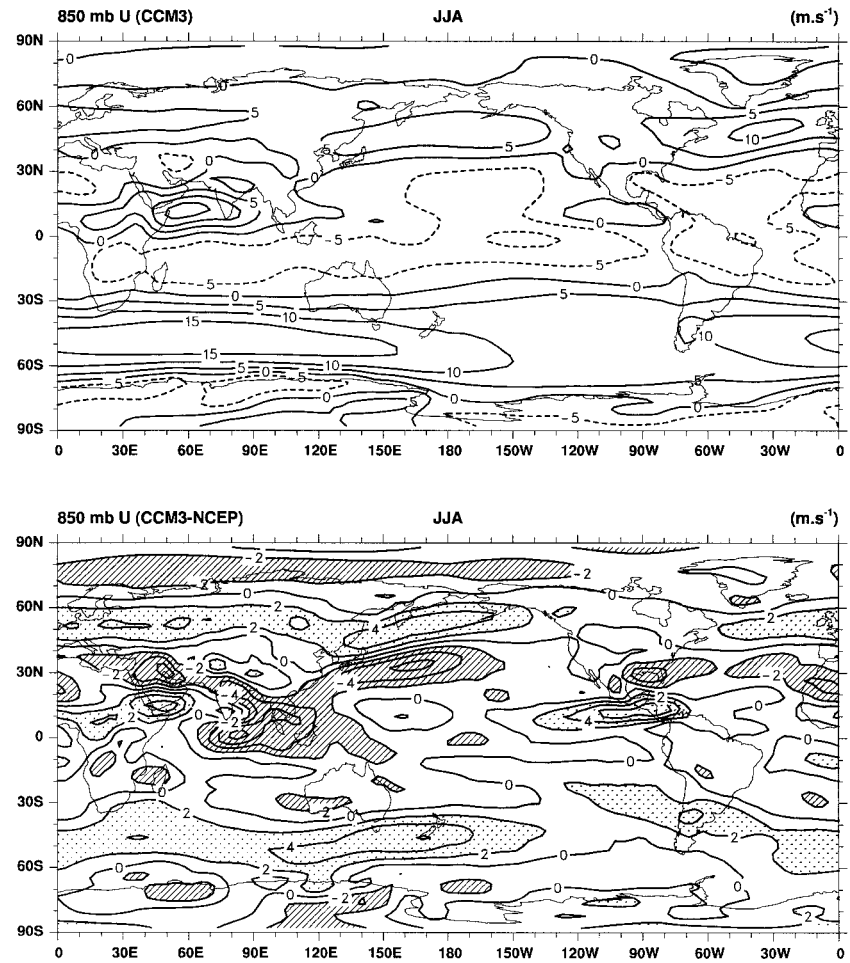


FIG. 15. As in Fig. 14 but for JJA.

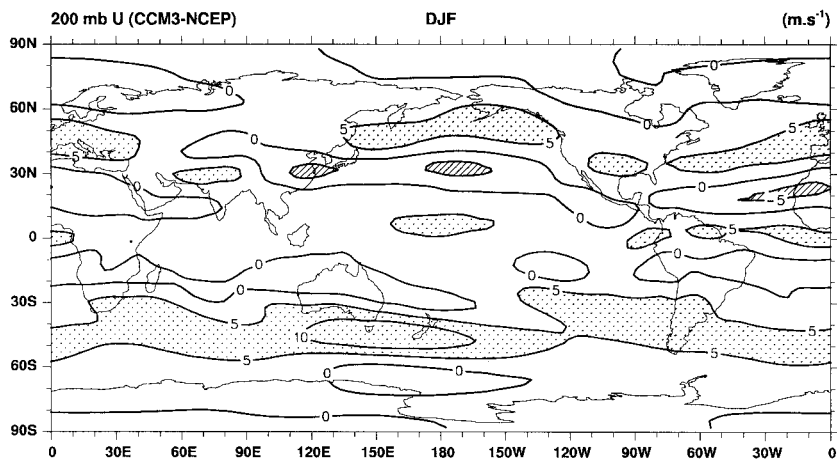
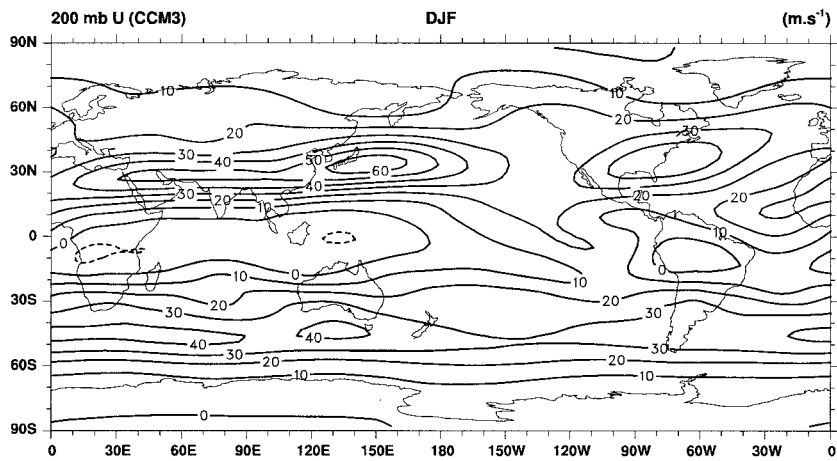


FIG. 16. Mean DJF 200-mb zonal wind from CCM3 (top) and differences from the NCEP climatology (bottom). The contour increment in the top panel is 10 m s^{-1} and easterlies are dashed. Differences are contoured every 5 m s^{-1} , values less than -5 m s^{-1} are hatched, and differences greater than 5 m s^{-1} are stippled.

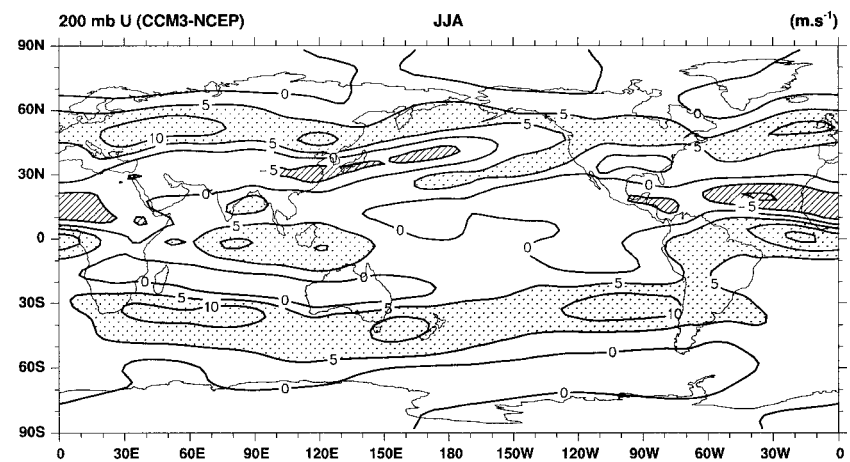
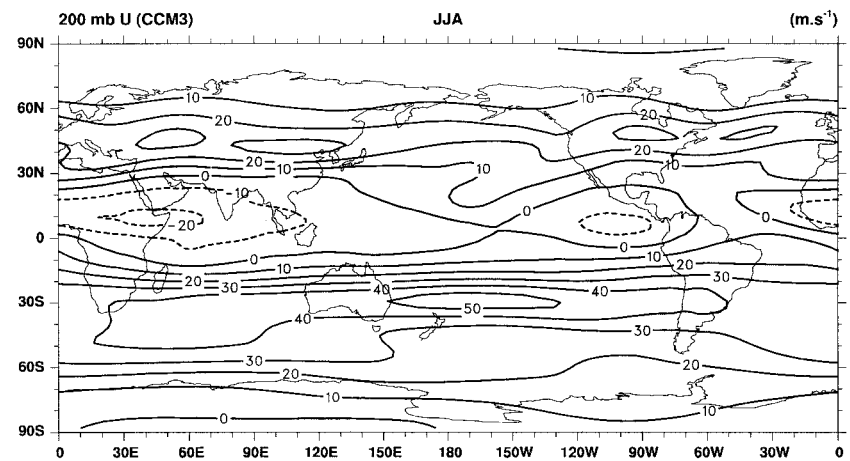


FIG. 17. As in Fig. 16 but for JJA.

simulated easterlies are too far north by nearly 10° lat producing a westerly error centered near the equator.

A striking feature of the wintertime 200-mb zonal winds over the SH is a maximum near 30°S with values near 50 m s^{-1} over Australia and the Pacific, a feature well captured by CCM3 (Fig. 17). The strongest westerlies extend too far west over the Indian Ocean, however, and the simulated 200-mb westerlies near 40°S are about 8 m s^{-1} stronger on average than the NCEP data (Fig. 13). Notwithstanding this bias, the CCM3 successfully reproduces the observed spiraling of the maximum westerlies over the Indian Ocean through the middle latitudes to higher latitudes over the Pacific Ocean, resulting in relatively weaker westerlies (the split jet) over New Zealand.

d. Rotational flow

The rotational component of the flow, as depicted by the streamfunction, is a well-measured quantity. Moreover, by examining departures from the zonal symmetry (i.e., the eddy streamfunction), stationary wave patterns extending through the Tropics can be examined. Regional differences between the simulated and observed eddy streamfunction at 200 mb are shown in Figs. 18 and 19.

The major circulation centers in the upper troposphere during both seasons are simulated very well by CCM3. During northern winter, differences from the NCEP values are exceptionally small, a significant improvement over earlier CCM versions in which amplitude errors and phase shifts often resulted in local differences more than four times those shown in Fig. 18 (Hurrell et al. 1993; Kiehl et al. 1998b). In particular, the low-latitude anticyclonic couplet over the tropical western Pacific and the tropical cyclonic centers over the east Pacific and Atlantic are well simulated. The higher-latitude zonal asymmetries are much more pronounced over the NH than the SH, where CCM3 simulates the observed strong southerly flow to the west of the major ridges over western North America and the eastern Atlantic, and the strong northerlies to the west of troughs over Japan and Hudson Bay. The only differences from NCEP of note during DJF occur near the western Pacific anticyclonic couplet, which is too weak near the date line in the NH and is too strong over Australia, consistent with 200-mb zonal wind errors in these regions (Fig. 16).

During southern winter, the main features both observed and simulated by CCM3 include anticyclonic centers in the Eastern Hemisphere and subtropical troughs over the Pacific and Atlantic Oceans (Fig. 19). The zonal asymmetry is markedly smaller in the middle latitudes of the SH than at lower levels (not shown), although wave 1 is still evident, albeit with slightly greater amplitude than observed. The cyclonic center east of New Zealand is simulated, so that the westerlies over New Zealand are at a relative minimum (Fig. 17), and the flow has a strong southerly component from the

Indian Ocean across southern Australia. As for DJF, the JJA differences from NCEP are quite small and represent a striking improvement over earlier model versions. The most significant difference arises from a slight westward shift and underestimate of the upper-level anticyclone associated with the summer monsoon circulation, which is consistent with the westerly bias of nearly 10 m s^{-1} over the tropical Indian Ocean (Fig. 17). Other relative weaknesses are the simulated subtropical troughs over the Atlantic during JJA, which are stronger than observed in both hemispheres, and the underestimation by CCM3 of the observed cyclonic center over the eastern Pacific near 15°S (Fig. 19 bottom).

e. Surface wind stress

An important parameter for coupling AGCMs to dynamical ocean models is the surface wind stress (τ), by which the atmospheric winds drive the oceanic currents, and the ocean acts as a sink for atmospheric momentum. This field is a specified boundary condition in ocean general circulation models. Quantitative comparisons of simulated surface wind stress are complicated by uncertainties in observed values, large variations from year to year, and by differences in the bulk aerodynamic formulas used to evaluate stress values. Qualitatively, however, the main biases in CCM3 relative to the climatological estimates of Trenberth et al. (1990) are consistent with errors in the near-surface fields discussed previously.

The zonally averaged zonal component of the surface wind stress indicates that the strength of the trade winds in CCM3 is too strong (Fig. 20), consistent with higher than observed SLPs (Fig. 1) and latent heat fluxes (Kiehl et al. 1998a) throughout the subtropics during both seasons. The CCM3 surface stress also has an easterly bias up to 50°N , but it agrees more closely with observed estimates over the middle latitudes of the SH even though the circumpolar trough is too deep in the model. Locally, the largest biases occur over the northern oceans during winter (Fig. 21). The difference vectors are of greatest magnitude over the eastern Pacific and are consistent with a simulated Aleutian low that does not extend as far east as observed (Fig. 2). Similarly, the southerly bias over the North Atlantic is consistent with the shortcomings of the simulated Icelandic low discussed earlier, also evident in the 850-mb winds (Fig. 14). Over the tropical oceans the easterly biases are slight during both seasons, a considerable improvement over previous versions of the model especially over the central and western Pacific (Hurrell et al. 1993). At high southern latitudes the largest differences during summer occur south of New Zealand associated with erroneous low pressure (Fig. 2), while wintertime errors at these latitudes (Fig. 22) are consistent with the circumpolar trough being too deep and too far equatorward (Fig. 3). When coupled within CSM, however, the simulated surface stresses are improved between 50°S and 70°S dur-

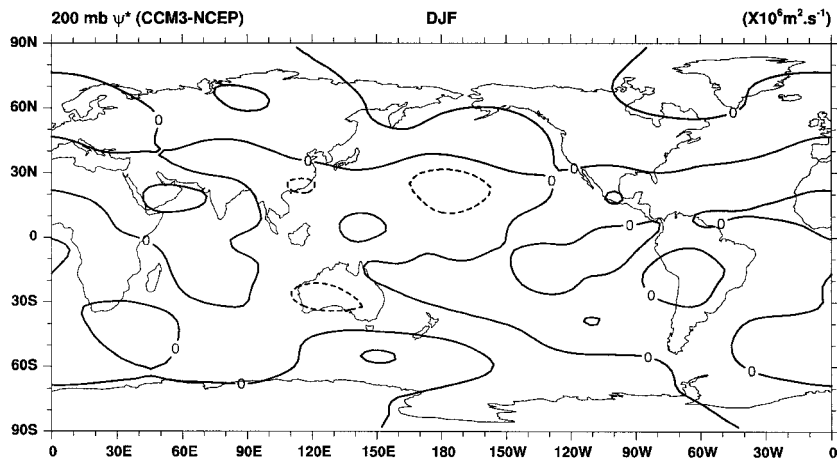
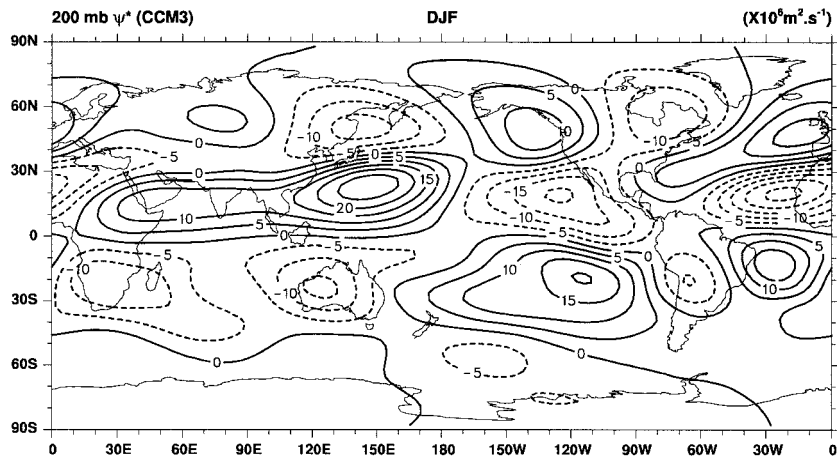


FIG. 18. Mean DJF 200-mb eddy streamfunction from CCM3 (top) and differences from the NCEP climatology (bottom). The contour increment in both panels is $5 \times 10^6 \text{ m}^2 \text{ s}^{-1}$ and negative values are dashed.

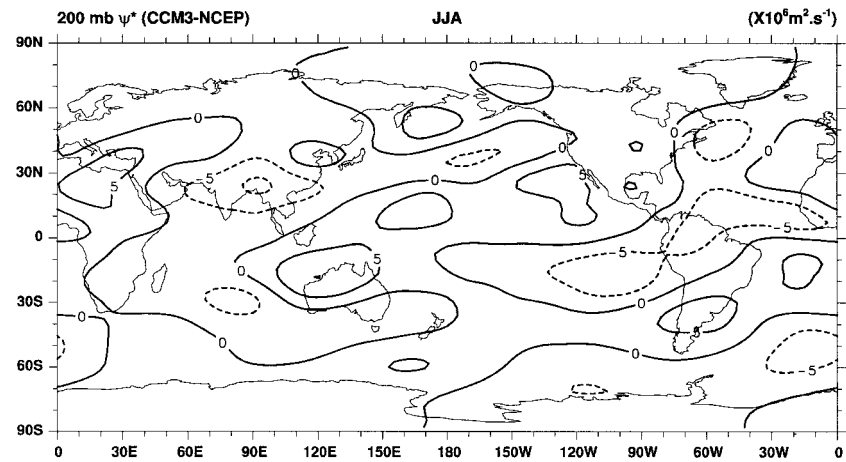
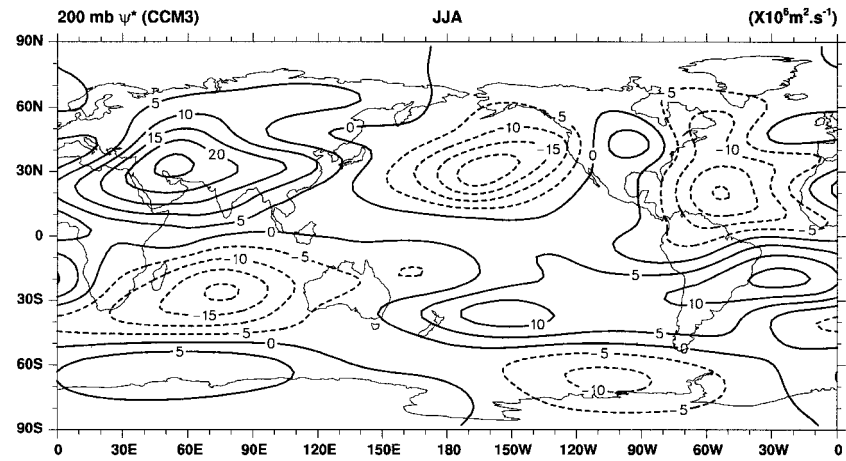


FIG. 19. As in Fig. 18 but for JJA.

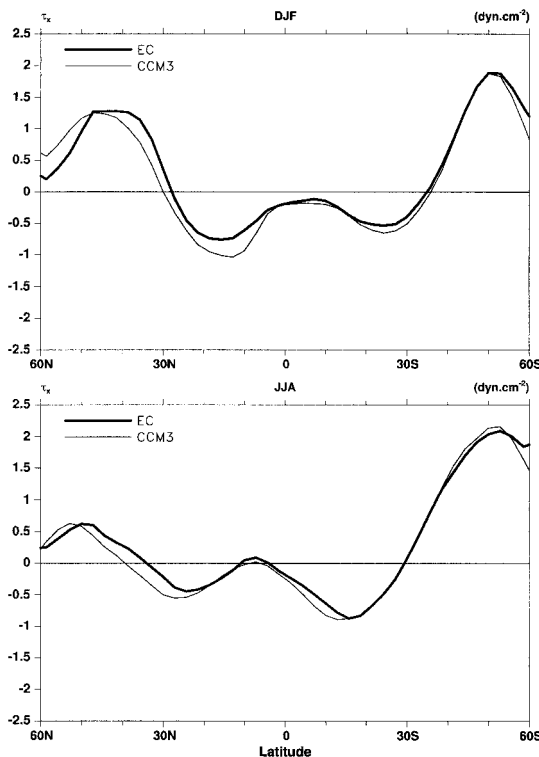


FIG. 20. Zonally averaged mean surface zonal wind stress (dyn cm^{-2}) for DJF (top) and JJA (bottom) from CCM3 (thin solid) and the ECMWF climatology (heavy solid).

ing JJA, presumably because of a realistic decrease in sea-ice area relative to the ice specified in the current simulation (Boville and Hurrell 1998).

f. Irrotational flow

The divergent (i.e., irrotational) component of the wind plays a much more prominent role in the Tropics than in higher latitudes. The analysis of observed divergence is sensitive to the initialization technique, to the numerical prediction model used for the data assimilation and, in particular, to the parameterizations of convection used in the assimilating model. While the magnitude of the analyzed divergent wind (or vertical motion) varies considerably among different global analyses, including the reanalyses, it is generally true that the patterns of divergence are more robust. For this reason, differences between CCM3 and NCEP should be viewed qualitatively.

To first order, the meridional circulation in the Tropics represents the direct response to diabatic heating. Seasonal plots of the zonal-mean meridional streamfunction simulated by CCM3 (Fig. 23) reveal a strong intensification and predominance of the winter Hadley cell in each hemisphere with mass fluxes of over $180 \times 10^9 \text{ kg s}^{-1}$. The center of the CCM3 circulation is near 700 mb in both seasons, somewhat lower than indicated by NCEP estimates (not shown). Qualitatively, CCM3 is

in better agreement with observational estimates than CCM2, which had too strong of a hydrologic cycle (Kiehl et al. 1998b; Hack et al. 1998) and placed the main centers of the Hadley cells about 10° lat farther south than CCM3 during DJF and about 5° lat farther north during JJA (see Hurrell et al. 1993).

The local divergent wind component and velocity potential at 200 mb from both NCEP and CCM3 are shown in Figs. 24 and 25. Note that total fields are presented and not difference maps, and vectors are plotted every third grid point. During northern winter, CCM3 simulates a broad band of tropical outflow, which extends zonally from the Indian Ocean to well east of the date line with the strongest flow from the SH into the NH. Strong upper-level divergence is also simulated over Africa and South America, with convergence over the eastern Pacific and Atlantic Oceans. All of these features are in good agreement with the NCEP reanalyses (Fig. 24), unlike previous versions of the model that were characterized by much more localized convergence and divergence centers. The primary differences are slightly weaker divergence over the tropical Indian Ocean and Brazil, and slightly stronger divergence near New Guinea. During southern winter, as observed, the strongest divergent flow is from the NH into the SH and emanates from a broad region of divergence centered near 15°N that stretches from India into the Pacific. Cross-equatorial flow is also well simulated over the eastern Pacific and Atlantic Oceans (Fig. 25). The most noticeable difference from NCEP during JJA is weaker simulated divergence over the Philippines.

g. Precipitation

The thermodynamic structure and hydrologic cycle of CCM3 is discussed in detail by Hack et al. (1998). Since precipitation is the result of links among the moisture, thermodynamics, and dynamics, however, the basic features of the CCM3 distribution are described briefly below.

Zonally averaged profiles of total precipitation are shown in Fig. 26. In northern winter, the maximum tropical precipitation in CCM3 is nearly 7 mm day^{-1} near 5°N , which is $\sim 2 \text{ mm day}^{-1}$ larger than the estimates of Xie and Arkin (1996). The model also does not simulate the observed maximum near 10°S , but rather has a broad peak extending to near 15°S . The subtropical minima are well simulated by CCM3, although they are lower than observations in the summer hemisphere and higher in the winter hemisphere. During both seasons, modeled precipitation rates are higher than the observational estimates over the middle-latitude storm tracks.

The large rainfall rates in the equatorial latitudes are associated with strong convection in the ITCZ, which migrates north and south in phase with the insolation, and these aspects are generally well simulated by CCM3. During DJF, the large rainfall rates associated with convection in the South Pacific and South Atlantic

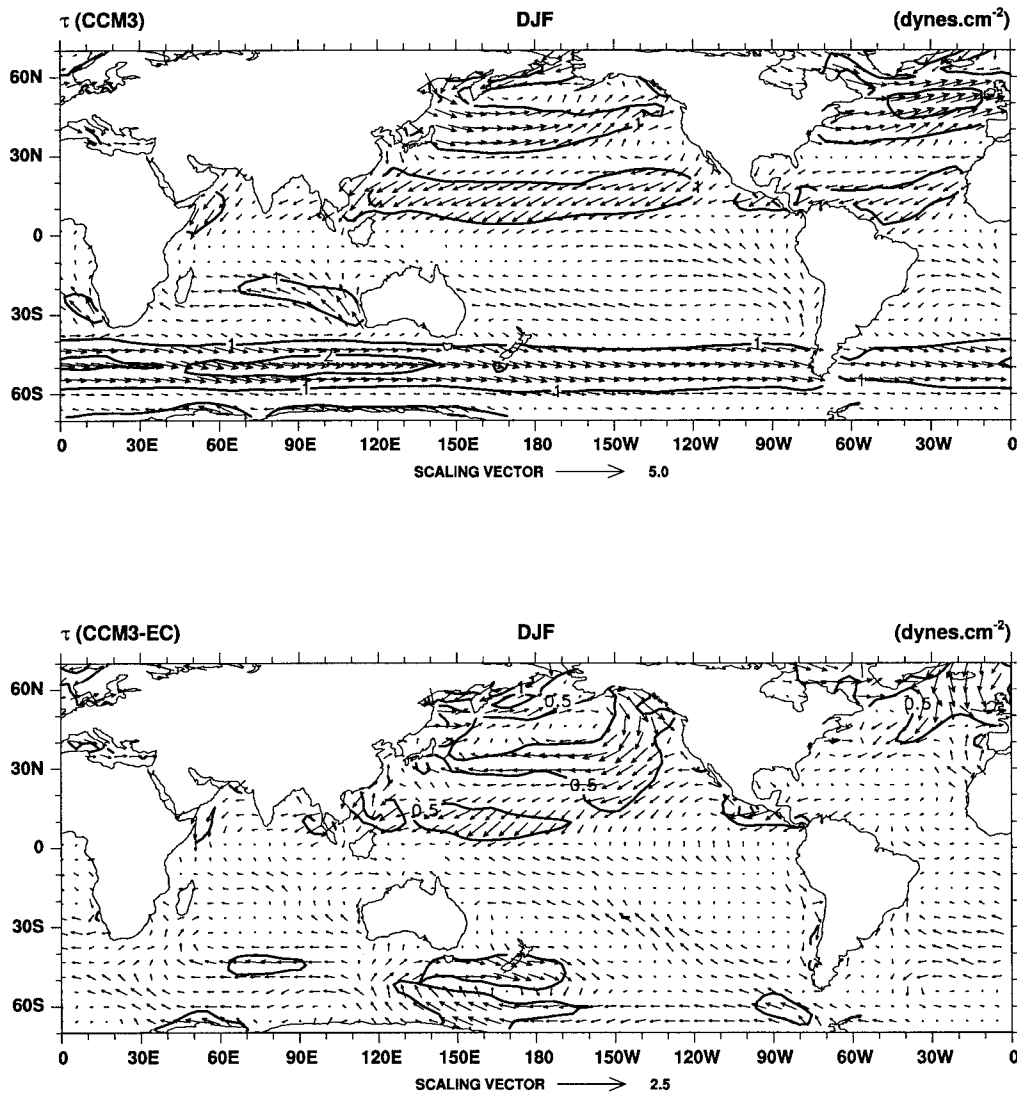


FIG. 21. Mean DJF surface wind stress vectors from CCM3 (top) and differences from the ECMWF climatology (bottom). The magnitudes are contoured every 1 (0.5) dyn cm^{-2} in the top (bottom) panel, and the largest vector corresponds to 5 (2.5) dyn cm^{-2} in the top (bottom) panel.

convergence zones are well captured by CCM3 and, as observed, they extend through the subtropics toward higher latitudes tapering to a minimum near 30°S (Fig. 27). Rainfall rates are much smaller during northern summer over these latitudes in both CCM3 and observations, when a clear and sharp maximum occurs near 10°N associated with the ITCZ (Fig. 28). The low precipitation rates over the subtropics with minima over the eastern parts of the oceans of both hemispheres are well simulated by CCM3. In agreement with the Xie and Arkin estimates, secondary maxima in precipitation are simulated over midlatitudes during winter where polar fronts and their associated disturbances predominate. The more zonal orientation in the SH than in the NH broadly reflects the different patterns of cyclone fre-

quency, although differences in the SH are more uncertain because of the lack of direct observations.

Consistent with realistic patterns and magnitudes of low-level divergence (not shown) and upper-level outflow (Figs. 24 and 25) simulated by CCM3, local differences in precipitation rates are generally small. Most notable during northern winter are the higher simulated rates just north of the equator near 150°E , over the eastern Pacific near 10°N , and over tropical Africa and the western Indian Ocean. Over the eastern Indian Ocean and the western Pacific, the zonally elongated maximum is to just north of the equator, compared to near 5°S in the observational estimates. During JJA, CCM3 precipitation rates are unrealistically high over the western Indian Ocean, the southeastern Arabian Peninsula, and

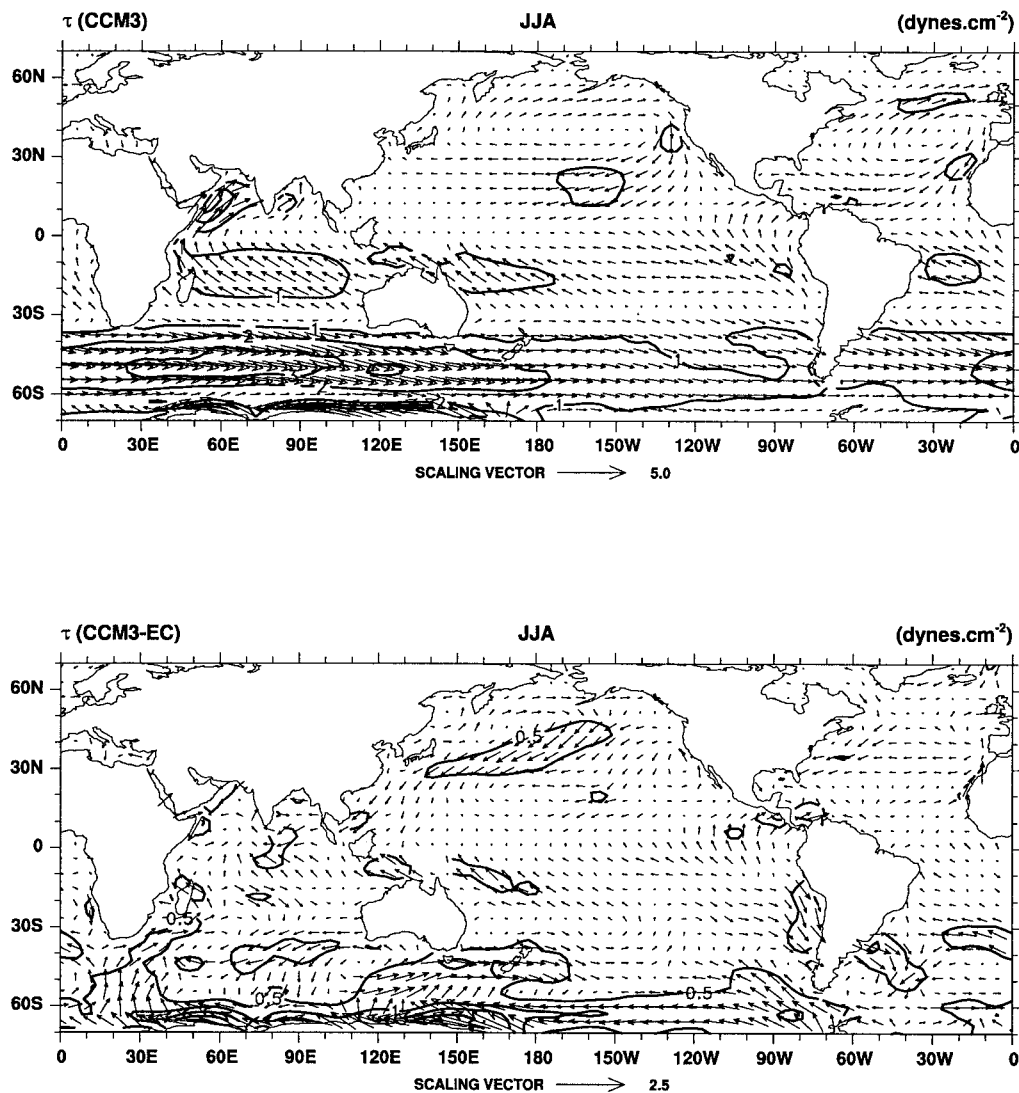


FIG. 22. As in Fig. 21 but for JJA.

the Caribbean Sea, but are too low near the Philippines and over the Pacific and Atlantic ITCZ. Overall, however, the simulated precipitation patterns represent a major improvement over preceding model versions (Hurrell et al. 1993; Kiehl et al. 1998b; Hack et al. 1998).

h. Eddy statistics

A brief look at the eddy statistics of CCM3 is presented through plots of the transient kinetic energy $\frac{1}{2}(\overline{u'^2} + \overline{v'^2})$ and the transient momentum flux $\overline{u'v'}$ at 250 mb, and the transient poleward heat flux $\overline{v'T'}$ at 850 mb. The variances and the covariances represent the mean daily variations about the seasonal mean (not the long-term mean), so that the interannual variability of the seasonal mean is not included. The plots presented, then, are simple averages of the 15-yr seasonal means.

The distribution of transient kinetic energy in the upper troposphere indicates the ability of the CCM3 to depict the main storm tracks. Many of the general features and the interseasonal changes are well simulated by CCM3. Over the NH during winter, the CCM3 produces a belt of maximum transient kinetic energy that extends from the Pacific across North America and the Atlantic into Europe (Fig. 29). During summer, the maximum values are weaker and shifted poleward of the wintertime belt by roughly 10° lat (Fig. 30). The simulated maximum transient kinetic energy over the SH encircles the globe between 40°S and 50°S during summer, but during winter it shifts equatorward over the Pacific and Atlantic Oceans and spirals poleward over the Indian Ocean toward the Pacific. The result is double maxima with minimum values over New Zealand, a feature also evident in the observed and simulated 200-mb zonal winds (Fig. 17). Over both hemispheres, the

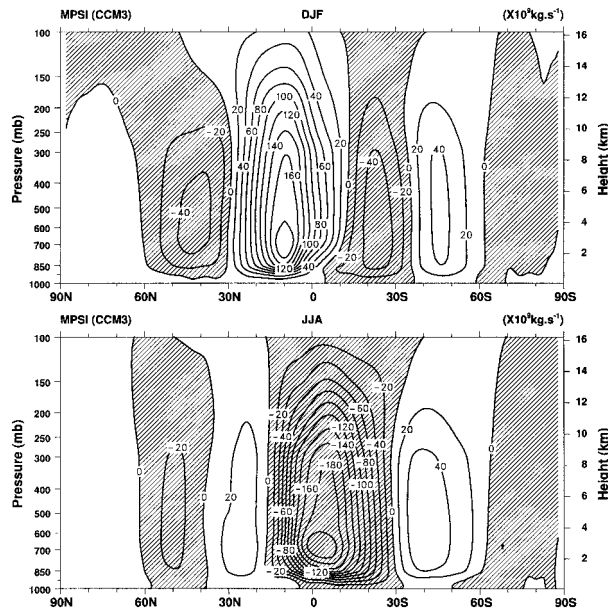


FIG. 23. Mean meridional streamfunction for DJF (top) and JJA (bottom) from CCM3. The contour increment is $20 \times 10^9 \text{ kg s}^{-1}$ and negative values are hatched.

belts of maximum transient kinetic energy expand latitudinally during winter, reflecting the enhanced daily meandering of the polar and subtropical jet streams.

A primary difference from observations is that the variability in the extratropical storm tracks is generally underestimated by CCM3, especially over the summer hemispheres. Similar results have been obtained for other AGCMs as well (e.g., Gates et al. 1990), including earlier versions of the NCAR CCM (Hurrell et al. 1993). The largest difference occurs over Australia during winter when CCM3 significantly underestimates the observed transient kinetic energy, which has a peak value of $300 \text{ m}^2 \text{ s}^{-2}$ (Fig. 30).

The model simulates the observed maxima in transient momentum flux in the upper troposphere over the southern United States and the Mediterranean during DJF, with secondary maxima over the northern oceans, and a band of high values centered near 40°S over the SH (Fig. 31). During JJA, the SH values increase in magnitude, while the transient momentum flux weakens over the NH as observed (Fig. 32). Overall, however, the simulated fluxes are too large over both hemispheres throughout the year. This is especially true of the two maxima over the NH during winter and over Eurasia during summer, and the enhanced momentum flux convergence relative to observations is consistent with the westerly wind biases evident at 200 mb in these regions (Figs. 16 and 17). Over the SH, the CCM3 transient momentum fluxes are much too strong over all three ocean basins, and this error increases into the stratosphere consistent with the westerly biases near 45°S in summer and 40°S in winter (Figs. 12 and 13).

In the lower troposphere, CCM3 successfully simu-

lates the major features and the interseasonal variations in the transient heat flux (Figs. 33 and 34). The most significant differences during DJF occur over the North Pacific, where the simulated maximum is too strong and too far poleward, consistent with the errors in the simulation of the Aleutian low (Fig. 2). Over the SH during JJA, the transient poleward heat fluxes are too weak over the subtropical Indian Ocean, but are too strong near 60°S across the hemisphere consistent with the deeper-than-observed circumpolar trough (Fig. 3).

i. Tropical intraseasonal oscillations

The tropical intraseasonal oscillation can be described, in simple terms, as a near-global-scale, quasi-periodic, eastward-moving disturbance evident in tropospheric temperature and winds over the equatorial belt. The oscillation substantially modulates tropical convection, especially over the Indian and western Pacific Oceans, and, consequently, impacts the extratropics as well. A simple way of examining the tropical intraseasonal variability in an AGCM is to examine longitude–time plots of daily precipitation, outgoing longwave radiation, or upper-tropospheric winds or velocity potential near the equator. The latter variable, at 200 mb averaged between 15°S and 15°N , is shown in Fig. 35 for December through May of two simulated years (1989/90 and 1990/91) from CCM3. The values were obtained by first removing the mean (15-yr) annual cycle from each daily value, then filtering the daily data to remove fluctuations with periods less than about one week.

A characteristic of the intraseasonal oscillation is that it displays considerable interannual variability, and the same is true of the 15-yr CCM3 simulation. As with most AGCMs (e.g., Slingo et al. 1996), the periodicity of the oscillation in CCM3 tends to be too short, nearer 20–30 days than 40–50 days as observed. Also, the observed phase speed is often faster over the Western Hemisphere (Weickmann and Khalsa 1990), a feature captured by CCM3 in some years but not others. These aspects are more clearly illustrated through time–longitude lag-correlation diagrams (Fig. 36).

For the two simulated northern winter and spring seasons shown in Fig. 35, an index of the oscillation is given by the 200-mb velocity potential averaged over the region 15°S – 15°N , 140° – 160°E . The structure of the oscillation is revealed by correlating the index with velocity potential at each longitude (averaged between 15°S and 15°N) with lags from -25 to $+25$ days. During the simulated year 1989/90 (Fig. 36 top), the periodicity of the oscillation is near 20 days and there is no change in phase speed between the Eastern and Western Hemispheres, which is characteristic of most AGCMs (Slingo et al. 1996). During the simulated year 1990/91 (Fig. 36 bottom), however, the periodicity is near 30 days and there is a clear change in phase speed near the dateline from $\sim 9 \text{ m s}^{-1}$ over the Eastern Hemi-

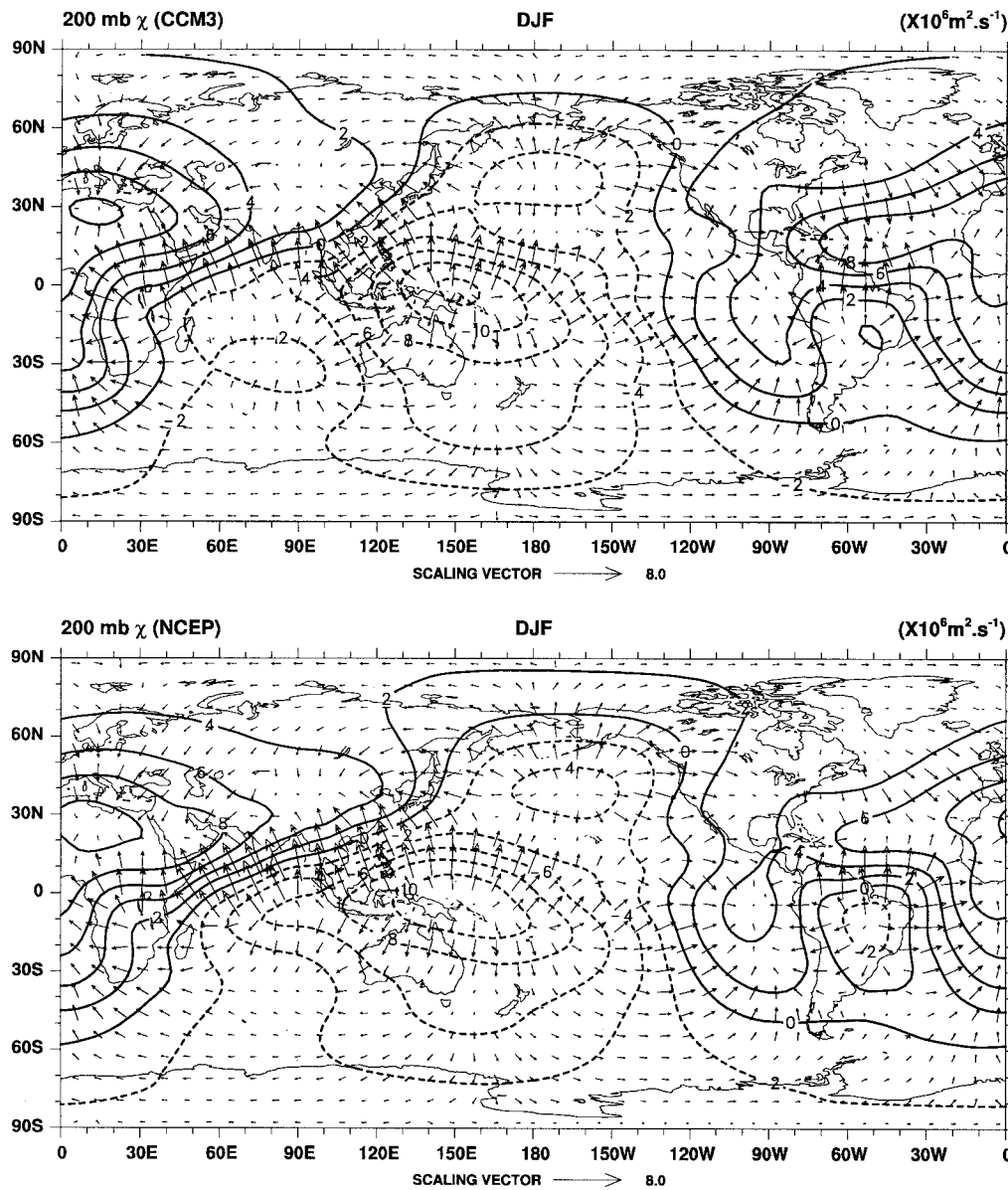


FIG. 24. Mean DJF velocity potential ($10^6 \text{ m}^2 \text{ s}^{-1}$) and vector divergent wind at 200 mb from CCM3 (top) and NCEP (bottom). Negative values of the velocity potential are dashed, and the largest vector corresponds to 8 m s^{-1} .

sphere (compared to an observed value near 6 m s^{-1} ; Weickmann and Khalsa 1990) to $\sim 19 \text{ m s}^{-1}$ over the Western Hemisphere (compared to $\sim 16 \text{ m s}^{-1}$). It is not clear why the change in phase speed occurs sporadically in CCM3. Waliser et al. (1998) have compared the tropical intraseasonal oscillation simulated by the Goddard Laboratory for Atmospheres (GLA) AGCM forced by specified annual cycle SSTs to an integration in which the GLA model was coupled to a slab ocean mixed layer model. They found that the simplified interactive SST yielded a more consistent reduction in the eastward phase speed over the Eastern Hemisphere and resulted in a better overall simulation

of the intraseasonal oscillation. The sensitivity of the oscillation in CCM3 to interactive SSTs is a topic of ongoing work.

An aspect well captured by CCM3 is a marked seasonality in the occurrence (not shown) of equatorially propagating intraseasonal events with greatest activity during northern winter and spring. However, the simulated amplitudes of the oscillations are considerably weaker than in CCM2, which was in good agreement with observed amplitudes (see Fig. 7 of Slingo et al. 1996). The extent to which this shortcoming is related to modifications of parameterized physical processes in CCM3 is currently being explored.

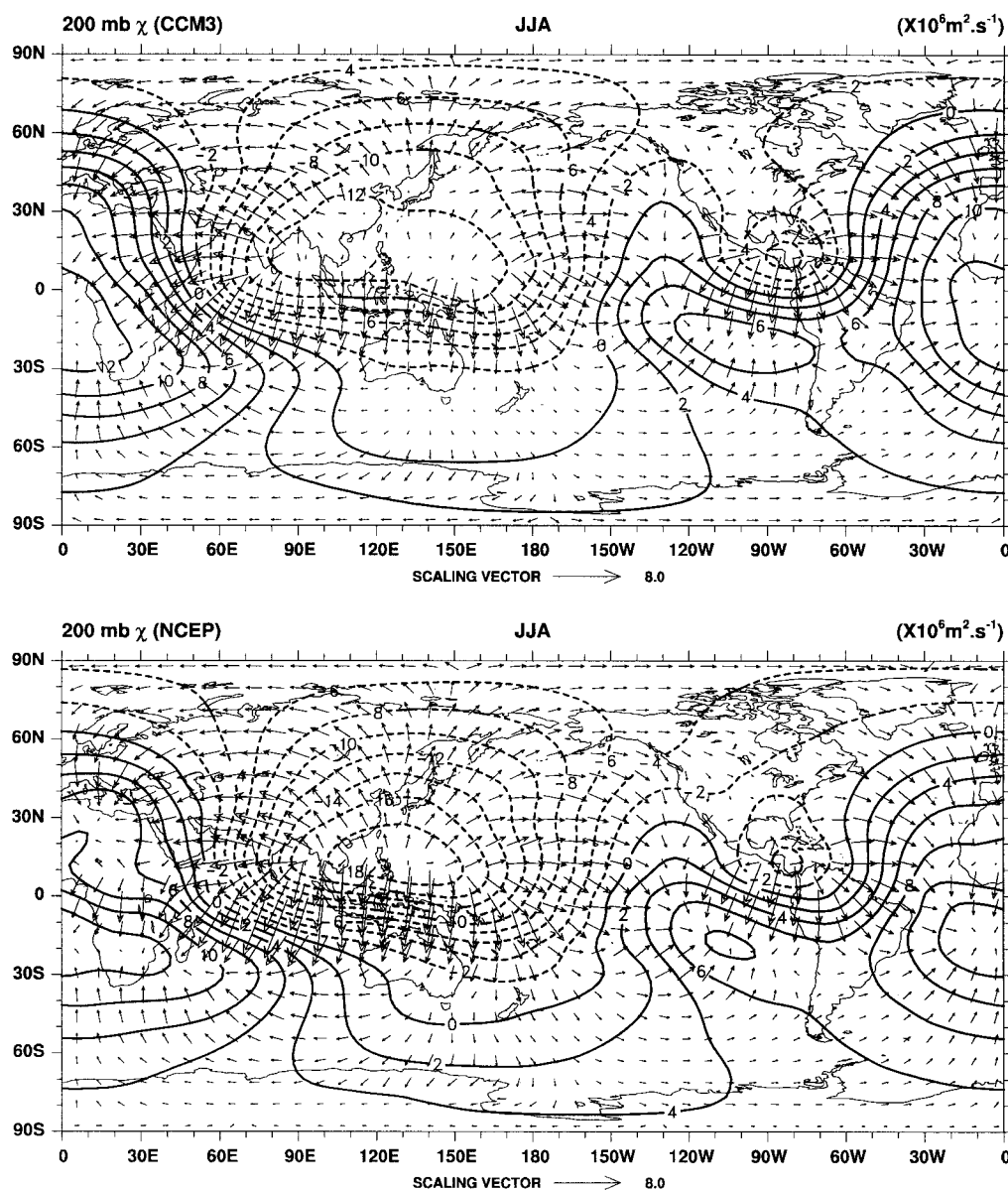


FIG. 25. As in Fig. 24 but for JJA.

j. Tropical interannual variability

Over the Tropics there is a fairly direct tropospheric response to SST anomalies, and there is a large interannual signal associated with El Niño–Southern Oscillation (ENSO). Also, unlike the extratropics, masking by natural internal atmospheric variability is small. For these reasons, the model's ability to realistically mimic the observed atmospheric variability associated with ENSO is briefly examined. Longitude–time series plots of tropical anomalies in outgoing longwave radiation and precipitation are presented in Kiehl et al. (1998a) and Hack et al. (1998), and both studies conclude the CCM3 does a very good job simulating the general structure and magnitude of the observed anomalies.

Variations in the Southern Oscillation (SO) can be measured from the inverse variations in pressures at Darwin (12.4°S, 130.9°E) in northern Australia and Tahiti (17.5°S, 149.6°W) in the South Pacific. Annual mean pressures at these two stations are correlated at -0.79 , and an index of the SO can be defined as $T_N - D_N$, where T and D refer to the departure from long-term monthly mean SLP at Tahiti and Darwin, respectively, and N represents the normalization by the annual mean standard deviation of each time series (Trenberth 1984). For CCM3, the grid points closest to these stations were selected from an ensemble of six 45-yr integrations forced with the reconstructed SST analyses of Smith et al. (1996) from 1950 through 1981, and the

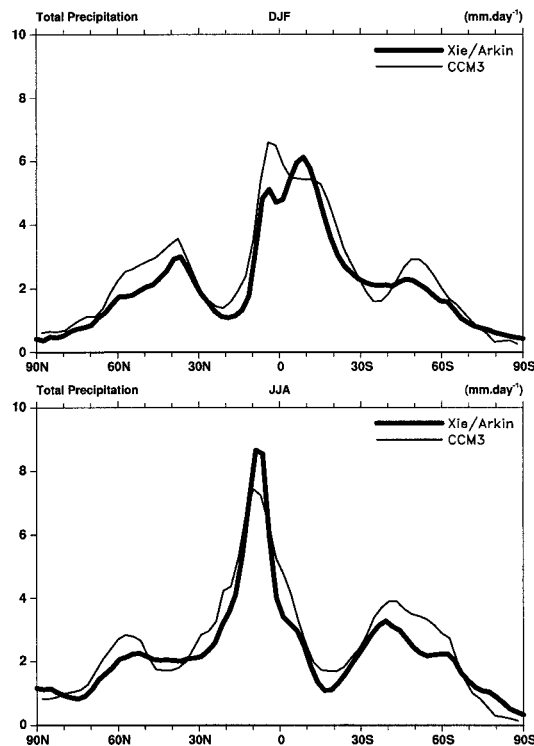


FIG. 26. Zonally averaged mean total precipitation (mm day^{-1}) for DJF (top) and JJA (bottom) from CCM3 (thin solid) and the observed climatology (heavy solid) of Xie and Arkin (1996).

optimally interpolated SST analyses of Reynolds and Smith (1994) through 1994.

The observed and simulated SO indices (Fig. 37) show good agreement, especially over several large excursions since 1950, and the spread of the six individual simulations is quite small, reinforcing the view that the tropical response to SST forcing is fairly deterministic. Observed shifts in tropical and subtropical convergence zones and monthly rainfall anomalies associated with variations in the observed SO index are also well simulated by the CCM3 (Fig. 38), in spite of the considerable uncertainties in the deduced observed values. Simulated rainfall anomalies over subtropical subsidence regions are more widespread and are larger than observed except over the western tropical Pacific, and the precipitation response over the equatorial central Pacific is slightly stronger than observed (see also Hack et al. 1998).

An example of the dynamical response to variations in tropical Pacific SSTs is given in Fig. 39, which shows simulated and observed differences in the DJF eddy streamfunction at 200 mb between the 1987 warm event and the 1989 cold event. The simulated response over the Western Hemisphere is quite good, indicating a realistic redistribution of the latent heat release over the modeled tropical Pacific atmosphere. In particular, the anomalous anticyclonic couplet over the tropical Pacific is well simulated, although slightly stronger and shifted

to the east of the observed anomalies. At higher latitudes, the response resembles the Pacific–North American teleconnection pattern, with anomalous cyclonic circulations over the Gulf of Alaska and the southeast United States, in agreement with the NCEP reanalyses.

5. Summary

Climate system models are needed to understand and consider simultaneously the wide range of complex interacting physical, chemical, and biological processes that characterize the atmosphere, ocean, and land. Before simulations from models such as CSM1 can be fully comprehended, however, it is necessary to understand the strengths and weaknesses of the component models. Atmospheric modeling at NCAR has a long history and the CCM has been an invaluable contribution to climate research for over a decade. This paper summarizes the dynamical aspects of simulations with the latest version of the model, CCM3, while Kiehl et al. (1998a), Hack et al. (1998), and Briegleb (1998) provide descriptions of the surface and top-of-the-atmosphere energy budgets, the thermodynamic structure and hydrologic cycle, and the simulated polar climate. Boville and Hurrell (1998) examine the changes in atmospheric circulation that occur when CCM3 is coupled within the NCAR CSM.

Many aspects of the CCM3 formulation and implementation are identical to the CCM2, although there are a number of important changes that have been incorporated into the collection of parameterized physics, along with some modest changes to the dynamical formalism (Kiehl et al. 1996). These changes have resulted in a clear improvement in the overall simulated climate of the model (e.g., Kiehl et al. 1998b). At sea level, the model reproduces the basic observed patterns of the pressure field quite well, including the major interseasonal changes in the subtropical high pressure centers and the higher-latitude low pressure systems. The SLPs throughout the subtropics of both hemispheres are higher than observed during DJF and JJA, however, whereas pressures in subpolar latitudes tend to be too low. The largest regional differences are on the order of 5 mb, about a factor of 2 less than in earlier CCM versions (e.g., Hurrell et al. 1993). Over the NH, SLP differences of this magnitude occur during winter where the simulated highs over the eastern Pacific and Atlantic Oceans are too strong, and erroneously low pressures at higher latitudes are most notable over Europe and Eurasia. Over the SH, the circumpolar Antarctic trough is too deep throughout the year, and the largest differences are found south of New Zealand where the model fails to capture the observed weakening and poleward shift of the maximum meridional pressure gradient.

The simulation of the middle-tropospheric flow is very good in CCM3, with regional differences from observations broadly consistent with the biases evident in the simulated SLP. The model successfully repro-

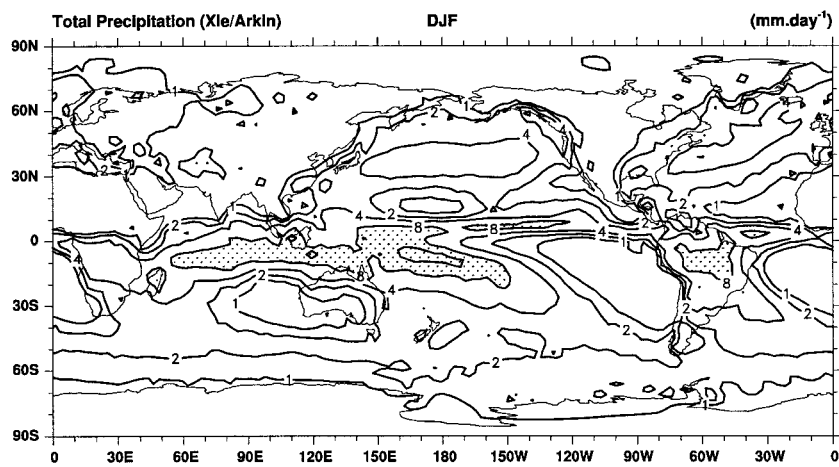
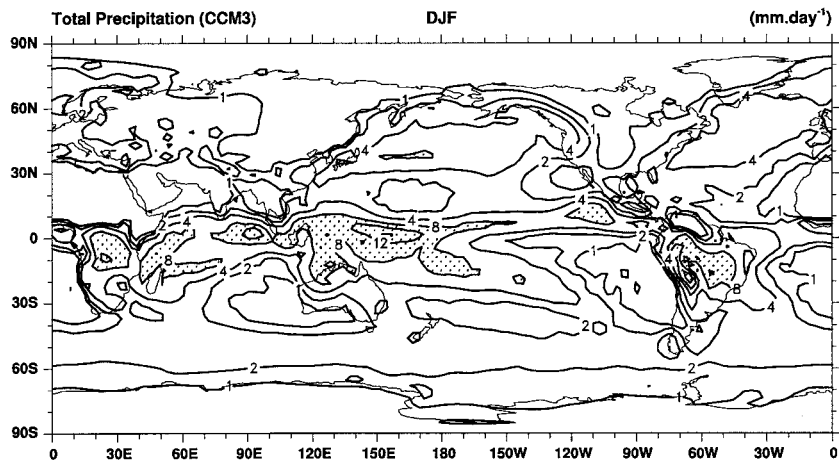


FIG. 27. Mean DJF total precipitation from CCM3 (top) and the Xie and Arkin (1996) climatology (bottom). The contours are 1, 2, 4, 8, 12, and 16 mm day⁻¹, and values greater than 8 mm day⁻¹ are stippled.

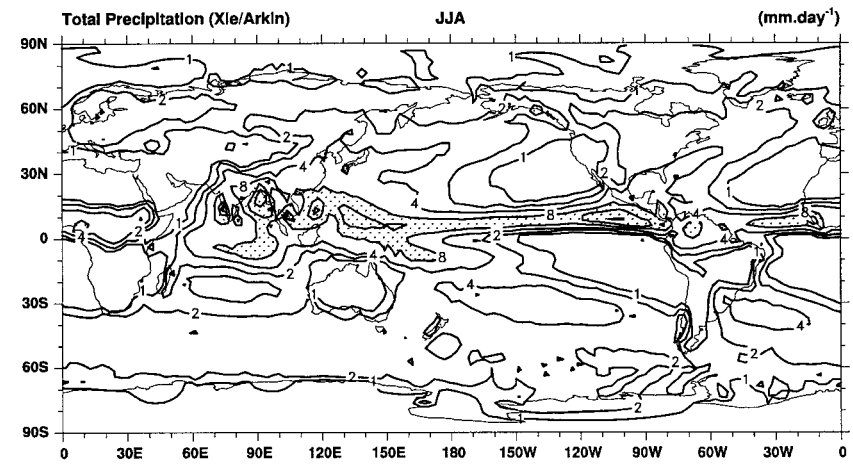
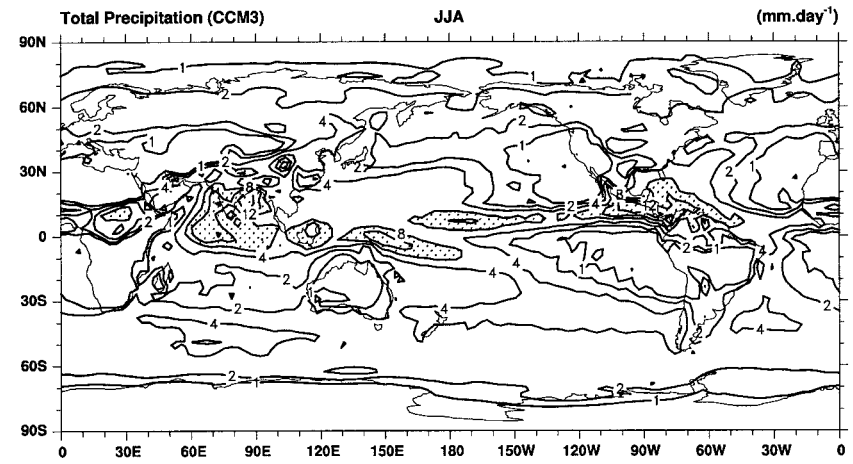


FIG. 28. As in Fig. 27 but for JJA.

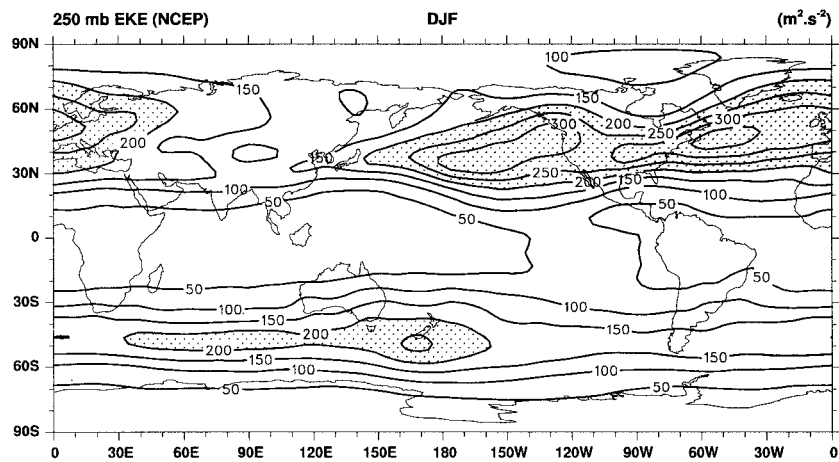
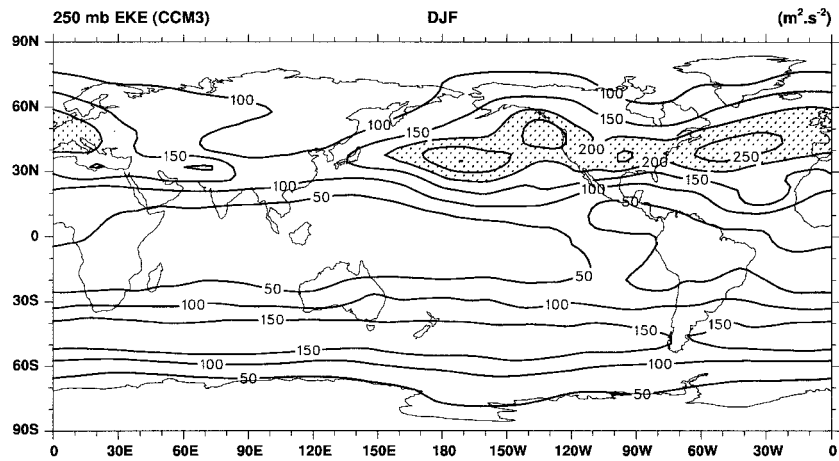


FIG. 29. Mean DJF transient kinetic energy at 250 mb from CCM3 (top) and NCEP (bottom). The contour increment is $50 \text{ m}^2 \text{ s}^{-2}$, and values greater than $200 \text{ m}^2 \text{ s}^{-2}$ are stippled.

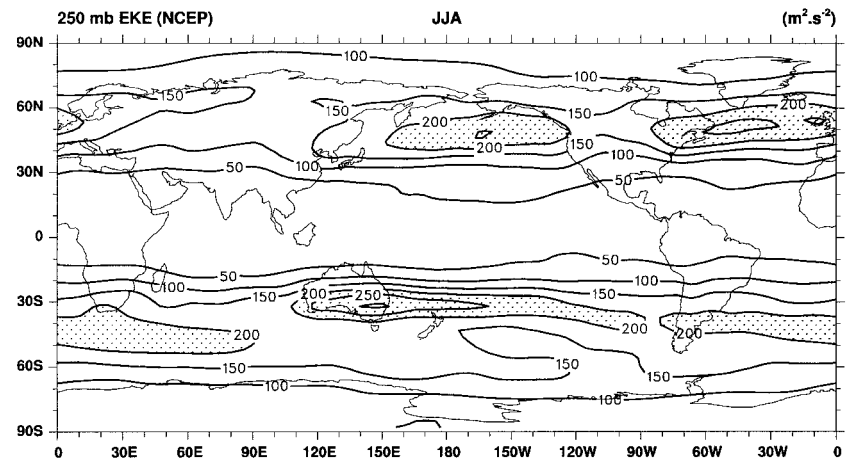
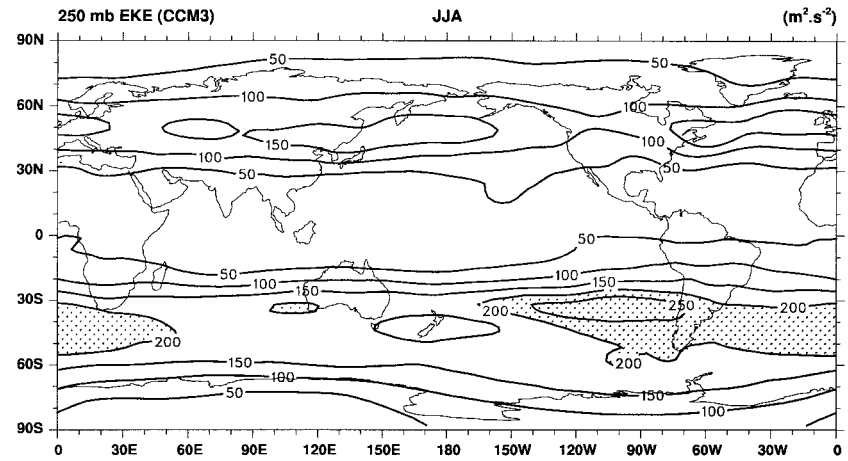


FIG. 30. As in Fig. 29 but for JJA.

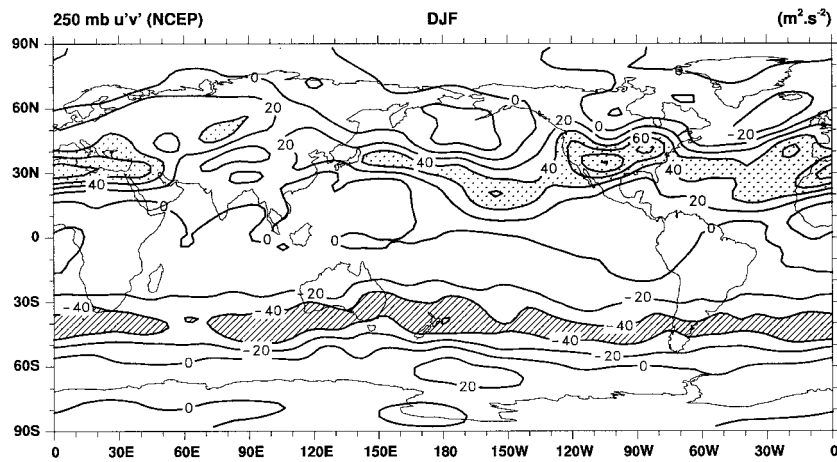
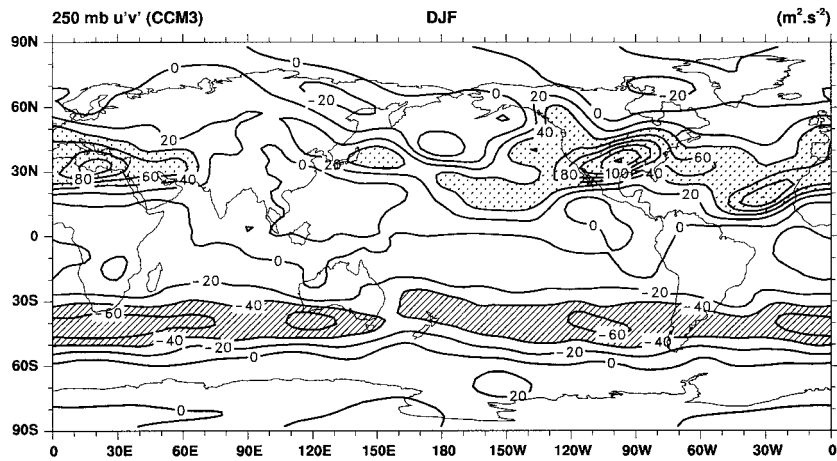


FIG. 31. Mean DJF transient momentum flux at 250 mb from CCM3 (top) and NCEP (bottom). The contour increment is $20 \text{ m}^2 \text{ s}^{-2}$, values less than $-40 \text{ m}^2 \text{ s}^{-2}$ are hatched, and values greater than $40 \text{ m}^2 \text{ s}^{-2}$ are stippled.

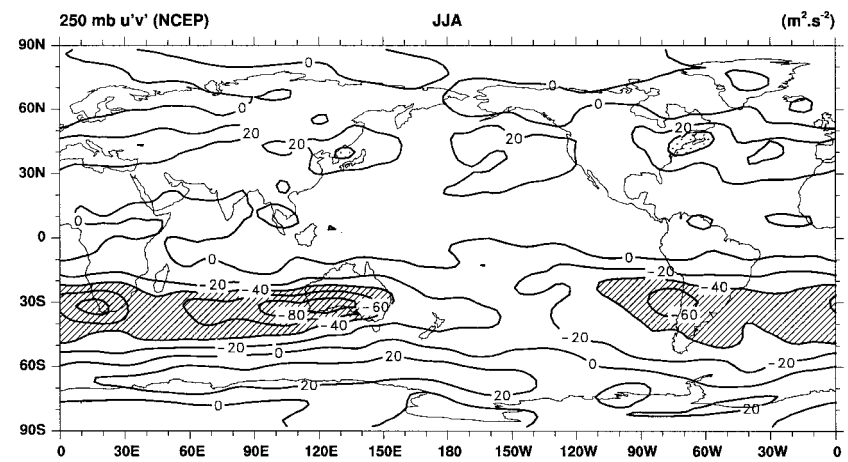
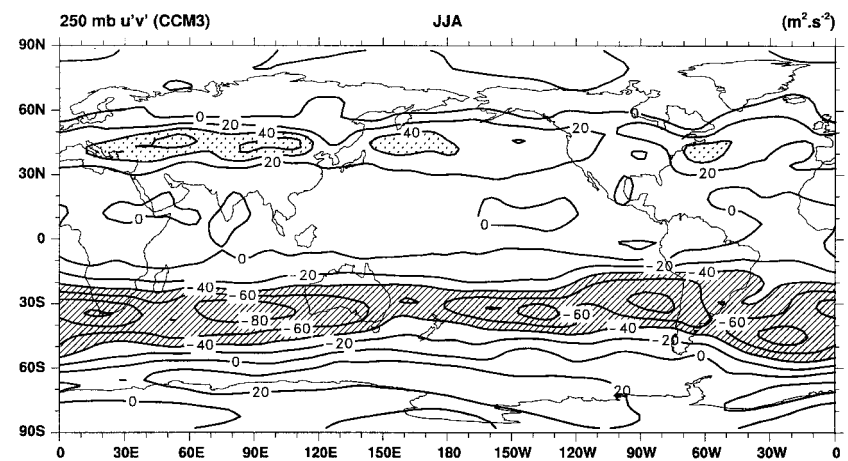


FIG. 32. As in Fig. 31 but for JJA.

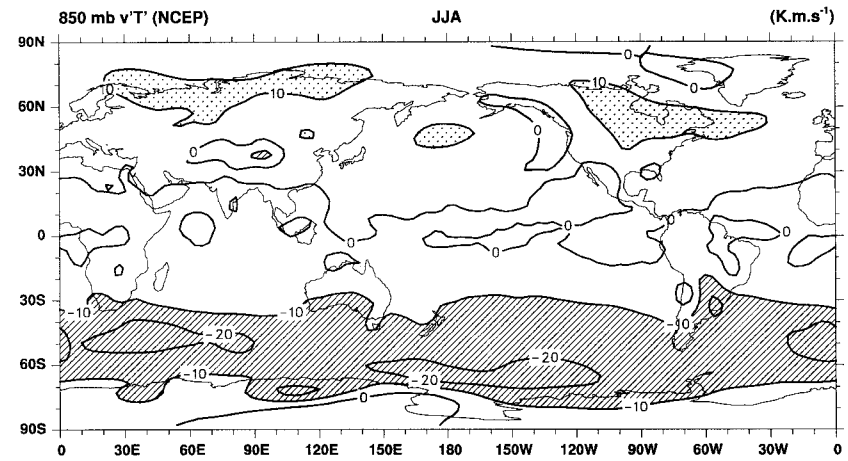
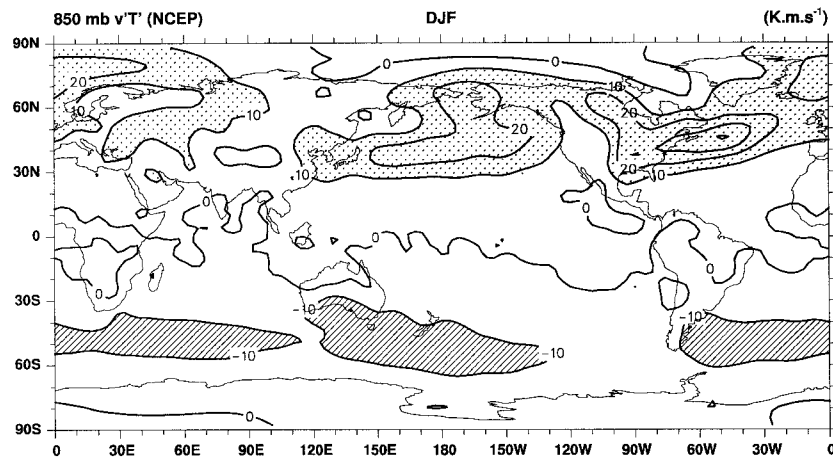
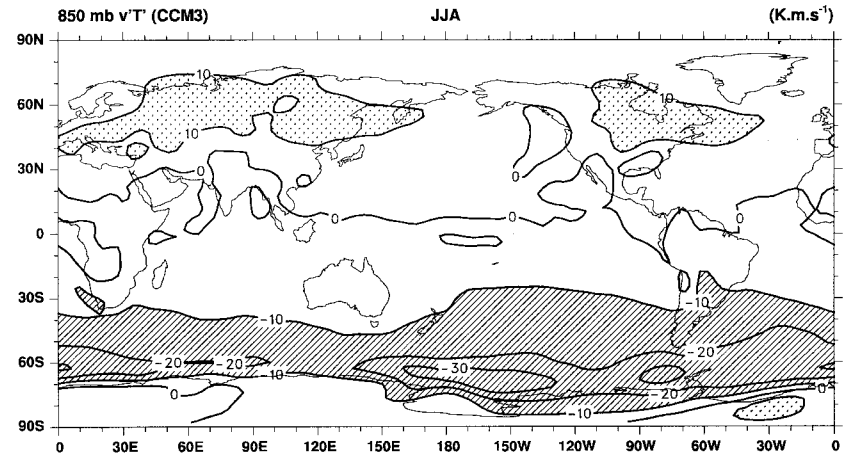
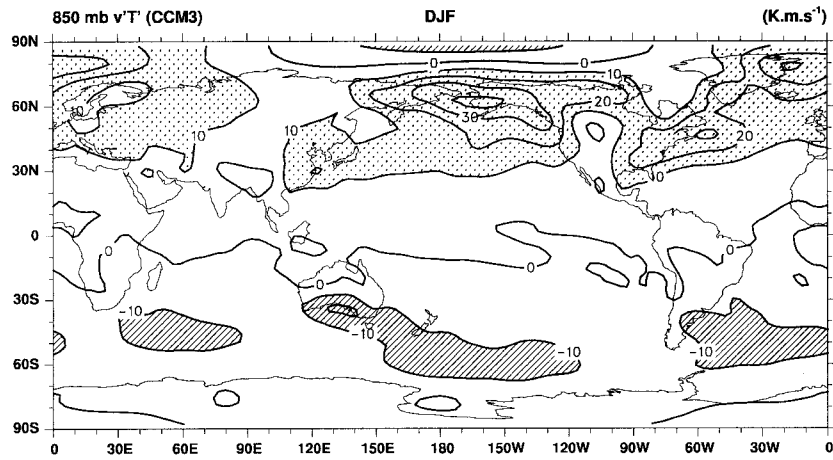


FIG. 33. Mean DJF transient heat flux at 850 mb from CCM3 (top) and NCEP (bottom). The contour increment is 10 K m s^{-1} , values less than -10 K m s^{-1} are hatched, and values greater than 10 K m s^{-1} are stippled.

FIG. 34. As in Fig. 33 but for JJA.

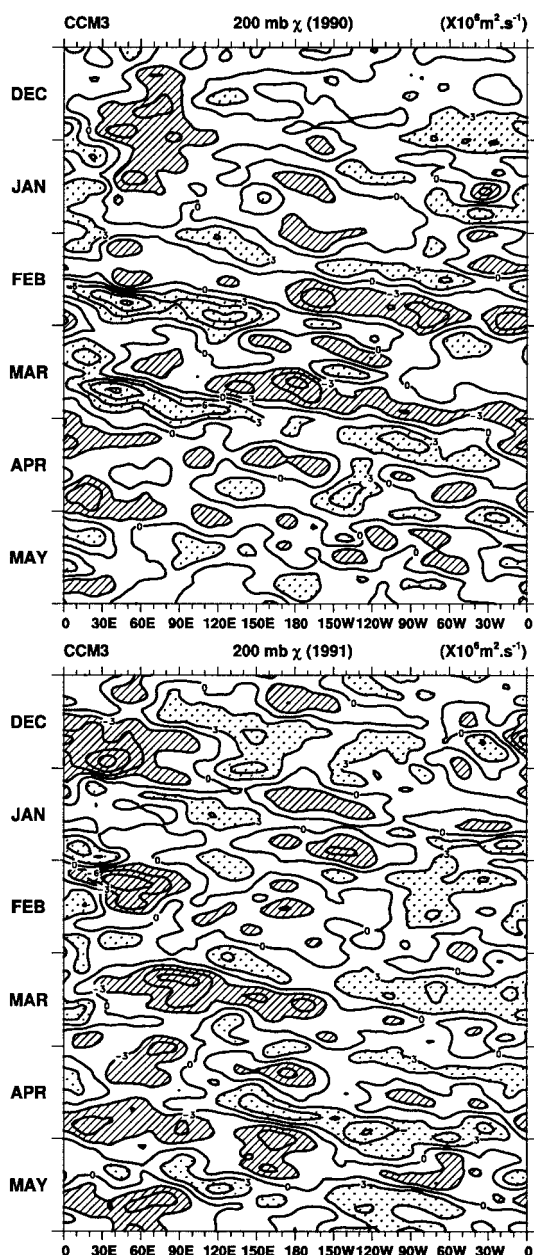


FIG. 35. Time-longitude diagrams (December–May) for the CCM3 simulated years 1989/90 and 1990/91 of the velocity potential at 200 mb, averaged between 15°S and 15°N . The contour increment is $3 \times 10^6 \text{ m}^2 \text{ s}^{-1}$, negative values are hatched, and positive values are stippled.

duces the observed large-scale zonal asymmetries at 500 mb, including the dominance of wavenumber 1 at high latitudes of the SH throughout the year, and the very large interseasonal changes in the quasi-stationary wave structure over the NH. The major shortcoming of the simulation is that CCM3 500-mb heights are lower than observed over the high latitudes of both hemispheres, consistent with a slight cold bias in the model (Hack et al. 1998).

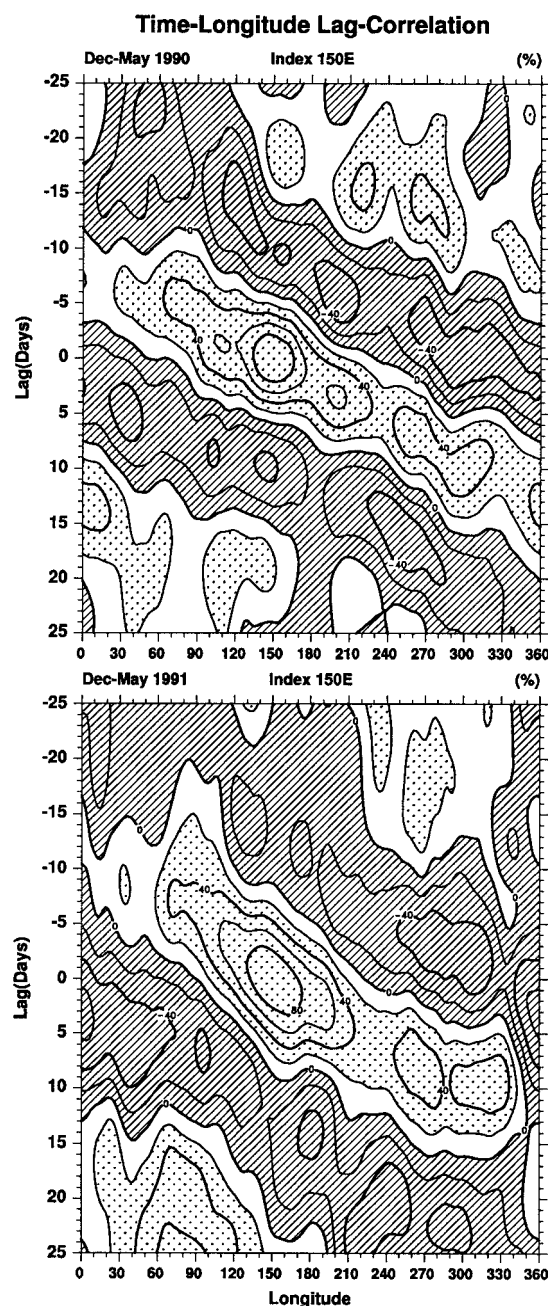


FIG. 36. Plots showing the lag correlations between an index of the tropical intraseasonal oscillation, given by the 200-mb velocity potential averaged over the region 15°S – 15°N , 140° – 160°E , and the 200-mb velocity potential at each longitude (averaged between 15°S and 15°N). The correlations are based on the daily values from December–May for the simulated years 1989/90 and 1990/91. The contour increment is 20%, negative correlations are hatched, and positive correlations are stippled.

The zonal wind structure in CCM3 is close to that of the NCEP reanalyses, although the middle-latitude westerlies are too strong between 40° and 50° lat of both hemispheres during both winter and summer. These westerly biases, which are consistent with errors in the

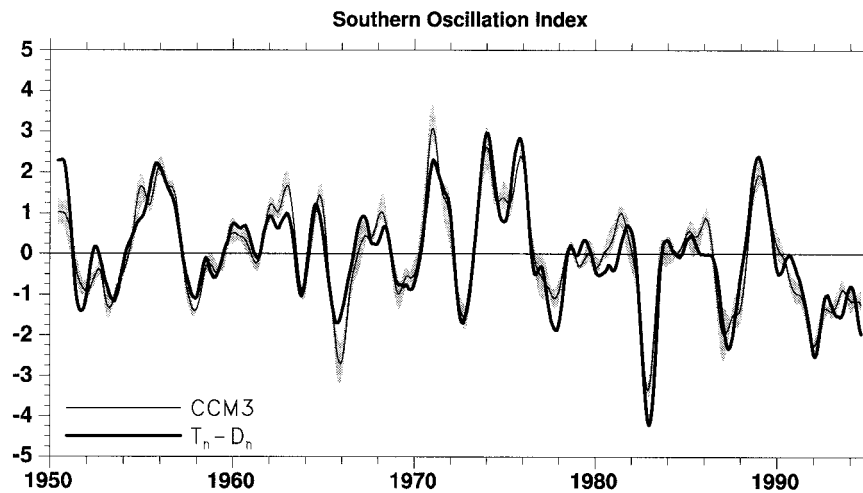


FIG. 37. Observed (heavy solid) and a six-member ensemble mean (thin solid) equivalent Southern Oscillation index from CCM3 integrations and the range about the means (stippled) since 1950. The values were smoothed with a low-pass 11-term filter that eliminates fluctuations of less than 8-month period but retains periods exceeding 24 months (Trenberth 1984).

pressure fields and the simulated transient momentum fluxes, are largest during southern winter and exceed 10 m s^{-1} in the zonal-mean upper troposphere over the SH. During northern winter, the zonally averaged westerly wind bias in the equatorial upper troposphere that plagued earlier versions of the model is much smaller ($\sim 4 \text{ m s}^{-1}$) in CCM3, in part reflecting an improved tropical hydrologic cycle and reduced Walker circulation (Hack et al. 1998; Kiehl et al. 1998b). Locally, over the tropical Pacific, the westerlies are stronger than observed by about 5 m s^{-1} near the date line, with an easterly bias of similar magnitude in the lower troposphere. The CCM3 trade winds are a bit stronger than observed, an error consistent with the enhanced subtropical high pressure centers in the model, and this leads to a slight easterly bias in the simulated surface wind stress. An overall view of the upper-tropospheric flow, as measured by the horizontal streamfunction, reveals that the major circulation centers and their interseasonal changes are very well simulated by the model, both in terms of magnitude and location. Local differences from NCEP reanalyses are up to a factor of 4 smaller than in previous versions of the NCAR CCM.

The observed patterns and magnitudes of upper-level divergent outflow are well simulated by CCM3, a finding consistent with an improved and overall realistic simulation of tropical precipitation. During northern winter, the CCM3 simulates the observed maxima in precipitation associated with the convergence zones over the South Pacific, South America, and Africa. Rainfall rates over the latter region are higher than observed, however, as are rates over the western Indian Ocean and just north of the equator over the western and far eastern tropical Pacific. In the zonal mean, CCM3 simulates an unrealistic maximum near 5°N , while during northern summer the maximum near 10°N is well captured. Pre-

cipitation rates are slightly lower than the observational estimates over the Pacific and Atlantic ITCZ in JJA, but are higher most notably over the western Indian Ocean, the Arabian Peninsula and the Caribbean Sea.

While our focus has been on the simulation of the mean state, the simulated variability of the CCM3 compares well to observations. For example, over the Tropics, the model simulates a clear eastward propagating anomaly in the tropical upper-tropospheric velocity potential, in qualitative agreement with the observed intraseasonal oscillation. This signal, which is also evident in the simulated zonal wind, precipitation, and outgoing longwave radiation fields, is characterized by large interannual variability and has a clear seasonal cycle with greatest activity during northern winter and spring. These features agree with observed characteristics of the oscillation. Typical periodicities, however, are near 20–30 days, which are shorter than observed, and the amplitudes of the oscillations are generally too weak. The CCM3 also appears to respond in a realistic manner to interannual variations in tropical SSTs (see also Kiehl et al. 1998; Hack et al. 1998). A simulated SO index agrees closely with the observed index dating back to 1950, and well-known changes in tropical and subtropical precipitation related to ENSO, together with associated anomalous wavetrains which extend into extratropical latitudes, are well simulated by the model.

Comparison studies such as this are only one approach to improve our understanding of the way models and the climate system behave. Given the enormous complexity of AGCMs, the simple identification of differences from observations does not easily translate into model improvements. Moreover, many other important aspects of the ability of the CCM3 to simulate the observed climate were not presented in this paper and are the topic of ongoing research. Examples include the

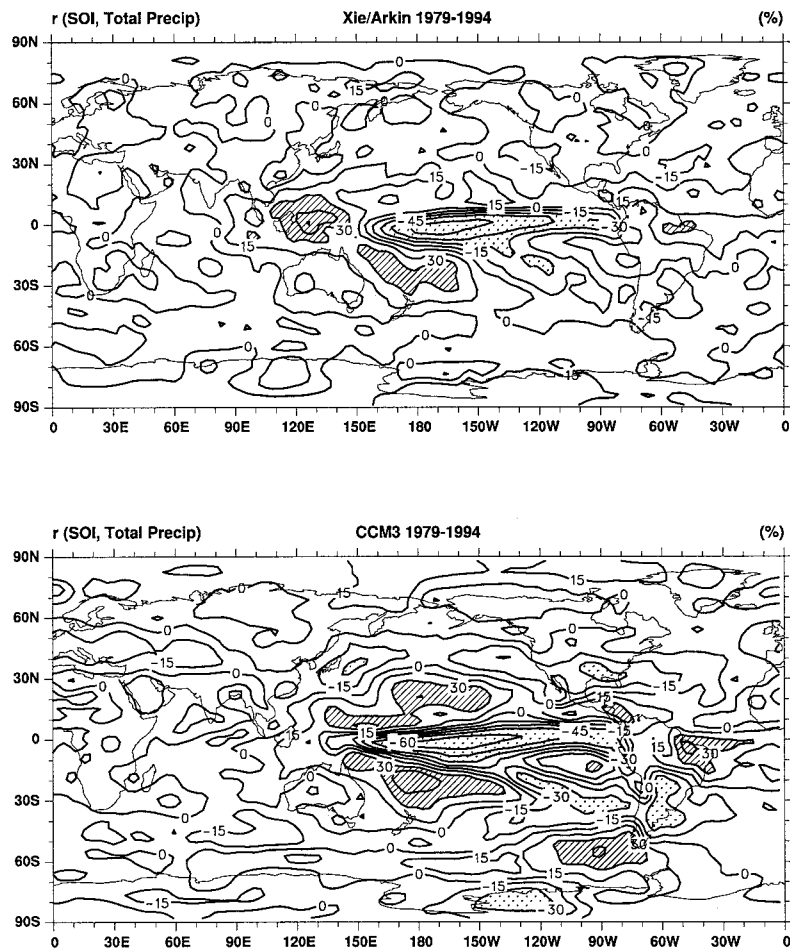


FIG. 38. Correlation coefficients (%) over 192 months (1979–94) between the observed Southern Oscillation index (as defined in the text) and (top) total precipitation from Xie and Arkin (1996) and (bottom) six-member ensemble mean anomalies from CCM3 integrations forced with observed global SSTs. Values less than -30% are stippled and values greater than 30% are hatched.

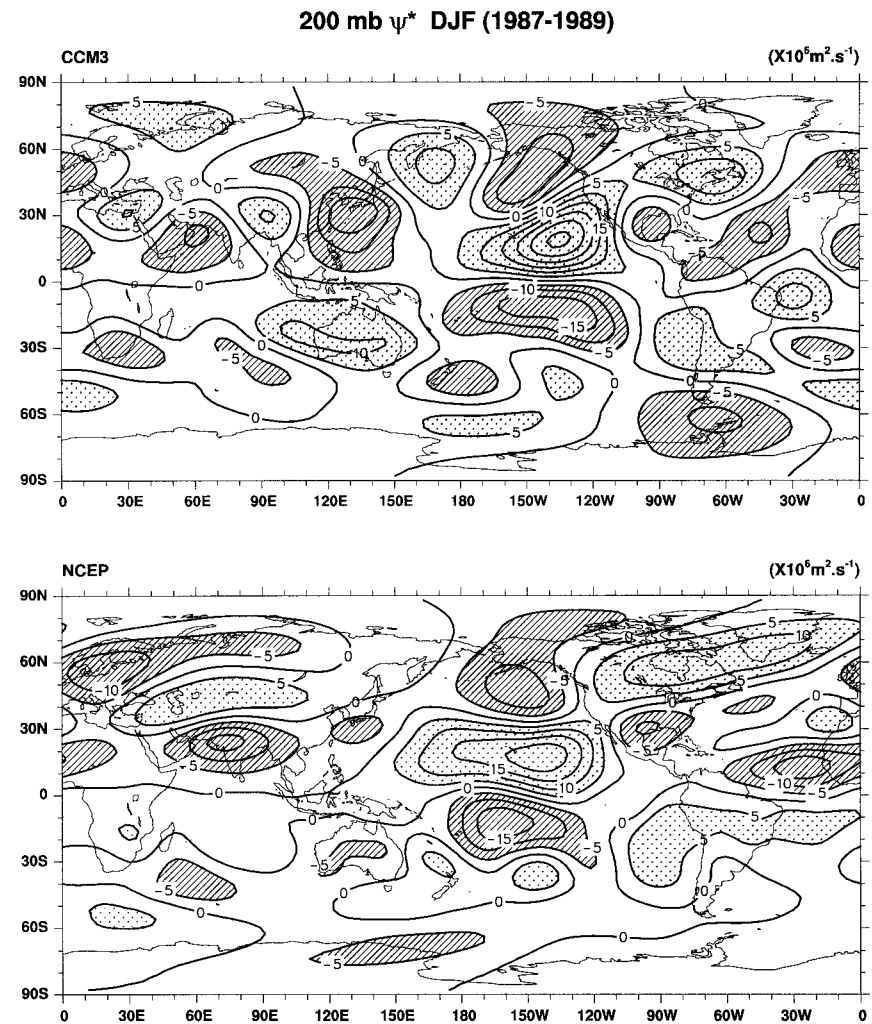


FIG. 39. The 200-mb eddy streamfunction difference between DJF 1987 and DJF 1989 from CCM3 (top) and NCEP (bottom). The contour increment is $5 \times 10^6 \text{ m}^2 \text{ s}^{-1}$, values less than $-5 \times 10^6 \text{ m}^2 \text{ s}^{-1}$ are hatched, and values greater than $5 \times 10^6 \text{ m}^2 \text{ s}^{-1}$ are stippled.

ability of the CCM3 to simulate observed variability on a wide array of timescales, and a more in-depth diagnosis of the simulated heat, momentum, and water budgets. Through such work, further progress on understanding the physical reasons behind the major simulation deficiencies will be made.

Acknowledgments. The authors gratefully acknowledge two anonymous reviewers for their helpful comments and suggestions, and we thank Liz Rothney for her help in preparing the manuscript.

REFERENCES

- Boer, G. J., and Coauthors, 1991: An intercomparison of the climates simulated by 14 atmospheric general circulation models. CAS/JSC Working Group on Numerical Experimentation. WCRP-58 WMO/TD-No. 425, World Meteorological Organization, Geneva, Switzerland.
- Bonan, G. B., 1996: A land surface model (LSM version 1.0) for ecological, hydrological, and atmospheric studies: Technical description and user's guide. NCAR Tech. Note NCAR/TN-417+STR, 150 pp. [Available from NCAR, Boulder, CO 80307.]
- Boville, B. A., and P. R. Gent, 1998: The NCAR Climate System Model, version one. *J. Climate*, **11**, 1115–1130.
- , and J. W. Hurrell, 1998: A comparison of the atmospheric circulations simulated by the CCM3 and CSM1. *J. Climate*, **11**, 1327–1341.
- Briegleb, B. P., and Bromwich, 1998: Polar climate simulation of the NCAR CCM3. *J. Climate*, **11**, 1270–1286.
- Gates, W. L., P. R. Rowntree, and Q.-C. Zeng, 1990: Validation of climate models. *Climate Change, The IPCC Scientific Assessment*, J. T. Houghton, G. J. Jenkins, and J. J. Ephraums, Eds., Cambridge University Press, 93–130.
- Hack, J. J., 1994: Parameterization of moist convection in the National Center for Atmospheric Research Community Climate Model (CCM2). *J. Geophys. Res.*, **99**, 5551–5568.
- , B. A. Boville, J. T. Kiehl, P. J. Rasch, and D. L. Williamson, 1994: Climate statistics from the NCAR Community Climate Model (CCM2). *J. Geophys. Res.*, **99**, 20 785–20 813.
- , J. T. Kiehl, and J. W. Hurrell, 1998: The hydrologic and thermodynamic characteristics of the NCAR CCM3. *J. Climate*, **11**, 1179–1206.
- Hurrell, J. W., J. J. Hack, and D. P. Baumhefner, 1993: Comparison of NCAR Community Climate Model (CCM) climates. NCAR Tech. Note NCAR/TN-395+STR, 335 pp. [Available from NCAR, Boulder, CO 80307.]
- , H. van Loon, and D. Shea, 1997: The mean state of the troposphere. *Meteorology of the Southern Hemisphere*, D. Karoly and D. Vincent, Eds., Amer. Meteor. Soc., in press.
- Kalnay, E., and Coauthors, 1996: The NCEP/NCAR 40-year reanalysis project. *Bull. Amer. Meteor. Soc.*, **77**, 437–471.
- Kiehl, J. T., J. J. Hack, G. B. Bonan, B. A. Boville, B. P. Briegleb, D. L. Williamson, and P. J. Rasch, 1996: Description of the NCAR Community Climate Model (CCM3). NCAR Tech. Note NCAR/TN-420+STR, 152 pp. [Available from NCAR, Boulder, CO 80307.]
- , —, and J. W. Hurrell, 1998a: The energy budget of the NCAR Community Climate Model: CCM3. *J. Climate*, **11**, 1151–1178.
- , —, G. B. Bonan, B. A. Boville, D. L. Williamson, and P. J. Rasch, 1998b: The National Center for Atmospheric Research Community Climate Model: CCM3. *J. Climate*, **11**, 1131–1149.
- Raphael, M., 1998: Quasi-stationary waves in the Southern Hemisphere: An examination of their simulation by the NCAR Climate System Model, with and without an interactive ocean. *J. Climate*, **11**, 1405–1418.
- Reynolds, R. W., and T. M. Smith, 1994: Improved global sea surface temperature analyses using optimum interpolation. *J. Climate*, **7**, 929–948.
- Slingo, J. M., and Coauthors, 1996: Intraseasonal oscillations in 15 atmospheric general circulation models: Results from an AMIP diagnostic subproject. *Climate Dyn.*, **12**, 325–357.
- Smith, T. M., R. W. Reynolds, R. E. Livezey, and D. C. Stokes, 1996: Reconstruction of historical sea surface temperatures using empirical orthogonal functions. *J. Climate*, **9**, 1403–1420.
- Sundqvist, H., 1988: Parameterization of condensation and associated clouds in models for weather prediction and general circulation simulation. *Physically Based Modelling and Simulation of Climate and Climatic Change*, M. E. Schlesinger, Ed., Kluwer Academic, 433–461.
- Trenberth, K. E., 1984: Signal versus noise in the Southern Oscillation. *Mon. Wea. Rev.*, **112**, 326–332.
- , 1992: Global analyses from ECMWF and atlas of 1000 to 10 mb circulation statistics. NCAR Tech. Note NCAR/TN-373+STR, 191 pp. + 24 fiche. [Available from NCAR, Boulder, CO 80307.]
- , W. G. Large, and J. G. Olson, 1990: The mean annual cycle in global ocean wind stress. *J. Phys. Oceanogr.*, **20**, 1742–1760.
- van Loon, H., 1972: Temperature, pressure, wind, cloudiness and precipitation in the Southern Hemisphere. *Meteorology of the Southern Hemisphere, Meteor. Monogr.*, No. 35, Amer. Meteor. Soc., 25–111.
- , 1984: The Southern Oscillation. Part III: Associations with the trades and with the trough in the westerlies of the South Pacific Ocean. *Mon. Wea. Rev.*, **112**, 947–954.
- Waliser, D. E., K. M. Lau, and J.-H. Kim, 1998: The influence of coupled sea surface temperatures on the Madden-Julian oscillation: A model perturbation experiment. *J. Atmos. Sci.*, in press.
- Weickmann, K. M., and S. J. S. Khalsa, 1990: The shift of convection from the Indian Ocean to the western Pacific Ocean during a 30–60 day oscillation. *Mon. Wea. Rev.*, **118**, 964–978.
- Xie, P., and P. A. Arkin, 1996: Analyses of global monthly precipitation using gauge observations, satellite estimates, and numerical model predictions. *J. Climate*, **9**, 840–858.
- Zhang, G. J., and N. A. McFarlane, 1995: Sensitivity of climate simulations to the parameterization of cumulus convection in the Canadian Climate Centre General Circulation Model. *Atmos.–Ocean*, **33**, 407–446.